The Fuchuan Ophiolite in South China: Evidence for Modern-Style Plate Tectonics During Rodinia Breakup

Si-Fang Huang[1,2], Wei Wang[1] , Andrew C. Kerr[2] , Jun-Hong Zhao[1], Qing Xiong[1], and Jian Wang[2]

[1]State Key Laboratory of Geological Processes and Mineral Resources, School of Earth Sciences, China University of Geosciences, Wuhan, China, [2]School of Earth and Environmental Sciences, Cardiff University, Cardiff, UK

Abstract Subduction initiation processes, such as those evidenced in the Izu-Bonin-Mariana (IBM) forearc crust are a key feature of modern-style plate tectonics. However, the evidence for this process in the Precambrian is limited, due to the scarcity of ophiolite suites and in particular a lack of typical complete ophiolitic sequences similar to those observed in Phanerozoic ophiolites. Mineral analyses of olivine, orthopyroxene, and chrome spinel from the harzburgite and two types of clinopyroxene from the cumulate gabbro of the Fuchuan ophiolite, South China suggest formation in a Neoproterozoic subduction system similar to the IBM. High temperature (1,000–1,200°C), low pressure along with a high degree of melt extraction (>18%) have been recorded in the harzburgite. This evidence, in conjunction with magma evolution from forearc basalt to boninite to hydrous calc-alkaline magmatism, recorded in the crustal section of the Fuchuan ophiolite indicates a transition from initial to mature subduction in a forearc setting. Statistical analysis of global ophiolites through time suggests that IBM-like subduction systems may have successfully operated since at least the latest Neoproterozoic (ca. 1,000 Ma) and be pervasive on Earth from ca. 850 Ma. Additional evidence for Neoproterozoic ophiolites from India, Siberia, and Arabian-Nubian Shield, which are also similar to the IBM forearc ophiolite, suggests that cold and deep subduction became much more common in the Neoproterozoic (ca. 850 Ma) around the periphery of the Rodinia supercontinent. This IBM-like subduction system may have acted as the geodynamic trigger for the break-up of Rodinia.

Plain Language Summary Earth is the only known planet with subduction zones and plate tectonics, and the timing of the onset of modern-style plate tectonics is still debated. An improved knowledge of modern-style plate tectonics is of vital significance to our understanding of Earth evolution. Neoproterozoic forearc ophiolite fragments from the periphery of Rodinia supercontinent are similar to the Izu-Bonin-Mariana forearc crust, suggesting that cold and deep subduction and modern-style plate tectonics may have developed in the Neoproterozoic (ca. 850 Ma) and thus may have acted as a trigger for the break-up of Rodinia.

1. Introduction

Earth is the only known planet with plate tectonics, which facilitates interaction between the lithosphere, hydrosphere, and atmosphere and has promoted the development of the biosphere. In the past few decades, however, proposed ages for the start of subduction span almost all of geological time before the Cambrian (Palin et al., 2020; and references therein). In recent years, plate tectonics *sensu lato* has been subdivided into modern-style and ancient-style (Zheng & Zhao, 2020). Modern-style plate tectonics is a response to cold and deep subduction (Stern, 2005; Zheng & Zhao, 2020), whereas the ancient-style is characterized by warm and shallow subduction related to bimodal geodynamic regimes (Palin et al., 2020; Zheng & Zhao, 2020). Modern-style plate tectonics is linked with secular cooling of the mantle, accompanied by changes in the buoyancy and rheology of ocean lithosphere, resulting in the horizontal motion of lithosphere and thus tectonic evolution similar to subduction (Cawood et al., 2018; Holder et al., 2019).

Ophiolites, representing fragments of oceanic crust and lithospheric mantle, have been tectonically incorporated into continental margins and can provide essential insights into the evolution of seafloor spreading, slab subduction, and plate tectonics (Dilek & Furnes, 2011, 2014; Khan et al., 2020). Well-preserved ophiolites are widespread throughout the Phanerozoic, but this is in contrast to the Precambrian where ophiolites

are sporadic and generally lack complete ophiolite stratigraphy sequences (Furnes et al., 2014). The best known Phanerozoic examples including the ca. 96 Ma Troodos ophiolite (Rioux et al., 2012), ca. 100 Ma Oman ophiolite (Ishikawa et al., 2002), and ca. 336–328 Ma Paleo-Asian Ocean ophiolite (Li et al., 2020) all have rock assemblages of highly depleted harzburgite, mid-ocean ridge-type basalt, boninite, and island arc lavas, similar to those found in the western Pacific Izu-Bonin-Mariana (IBM) intra-oceanic convergent margin (Coulthard et al., 2021; Reagan et al., 2010; Shervais et al., 2019). Although forearc basalts and high-Si boninites are considered to be particularly characteristic of subduction initiation, low-Si boninites are also linked with modern-style subduction settings (Pearce & Arculus, 2021; Pearce & Reagan, 2019; Resing et al., 2011). Therefore, the geochemical stratigraphy of ophiolite assemblages with forearc basalt, boninite, and calc-alkaline island arc lava (similar to the IBM arc) could represent a fundamental characteristic of forearc crust and therefore be a critical indicator of cold and deep subduction initiation. Consequently, the global formation of IBM-like ophiolites is considered as a critical proxy for the onset of modern-style plate tectonics (Dilek & Furnes, 2014; Ishizuka et al., 2014; Pearce & Robinson, 2010).

The Fuchuan ophiolite is found in South China along the Neoproterozoic (850–825 Ma) collisional suture between the Yangtze and Cathaysia blocks. In this article, we report new geochemical data from olivine, orthopyroxene, and chrome spinel in harzburgite, and clinopyroxene in the cumulate gabbro. As we will show, these data suggest that forearc basaltic and boninitic magmas were originally derived from highly depleted harzburgite with subsequent overprinting by slab fluids during subduction initiation. These geochemical features indicate that the stratigraphic sequences in the Fuchuan ophiolite are analogs of modern forearc oceanic lithosphere, despite being only partially preserved. A compilation of global ophiolites in Precambrian suggests that IBM-like subduction systems can be found in the geological record from ca. 1,000 Ma and likely represent evidence for the onset of modern-style plate tectonics since at least the latest Neoproterozoic.

2. The Fuchuan Ophiolite in South China and Sampling

South China Craton was formed through amalgamation between the Yangtze and Cathaysia blocks in the Neoproterozoic, with the Fuchuan ophiolite representing a significant component in the eastern suture zone (Figure 1; Li et al., 2009; Liu et al., 2020; W. Wang et al., 2019; W. Wang et al., 2013, X. L. Wang et al., 2013; Yao et al., 2019; Zhang et al., 2020; Zhao & Cawood, 2012; Zhao et al., 2011, 2012). The Fuchuan ophiolite extends for more than 50 km and formed at ca. 850–825 Ma. The ophiolite shows a relatively complete ophiolite sequence, including serpentinized harzburgite, pyroxenite, and serpentinite in some localities in its mantle section, along with pillow lava, fine-grained basalt, and cumulate pegmatitic gabbro in its crustal section (Figure 1; Zhang et al., 2012; C. L. Zhang et al., 2013). Some gabbroic and granitoid sills/dykes intrude into the ophiolite sequence and podiform chromitites occasionally occur within the serpentinized harzburgite (Figure 1; Shu et al., 2019). This ophiolite suite was obducted into the Neoproterozoic autochthonous sediment of the Shangxi Group. They are unconformably overlain by the Neoproterozoic Likou Group (Ding et al., 2008; Huang et al., 2018, 2019; Shu et al., 2019). Although the Fuchuan ophiolite has relatively intact rock sequences, significant differences in elemental and isotopic geochemistry between the mantle and crustal sections result in several tectonic models proposed based on different rock units, including island arc (lava unit), forearc (highly depleted harzburgite), and back-arc marginal sea (N-MORB gabbro; Li & Zhao, 2020; Shu et al., 2019; Zhang et al., 2012; C. L. Zhang et al., 2013).

Harzburgite and cumulate gabbro from the Fuchuan ophiolite were collected for this study. The harzburgite has been extensively serpentinized with only a minor amount of fresh olivine (<0.5 mm), orthopyroxene (<5 mm), chrome spinel, and occasional clinopyroxene being preserved (Figures 2a–2c). The chrome spinel grains are red-brown in thin sections and anhedral and are extensively cracked (Figure 2d). The cumulate gabbro comprises clinopyroxene and plagioclase, with no olivine, orthopyroxene, or magnetite being observed. Clinopyroxene grains of variable size, from less than 1 mm to several centimeters, from the cumulate gabbro, are well preserved and fresh with no indication of a metamorphic imprints, such as plastic deformation and palimpsest textures. However, plagioclase grains have been extensively altered (Figures 2e and 2f). Two cumulate gabbro samples were prepared for LA-ICP-MS zircon U-Pb dating.
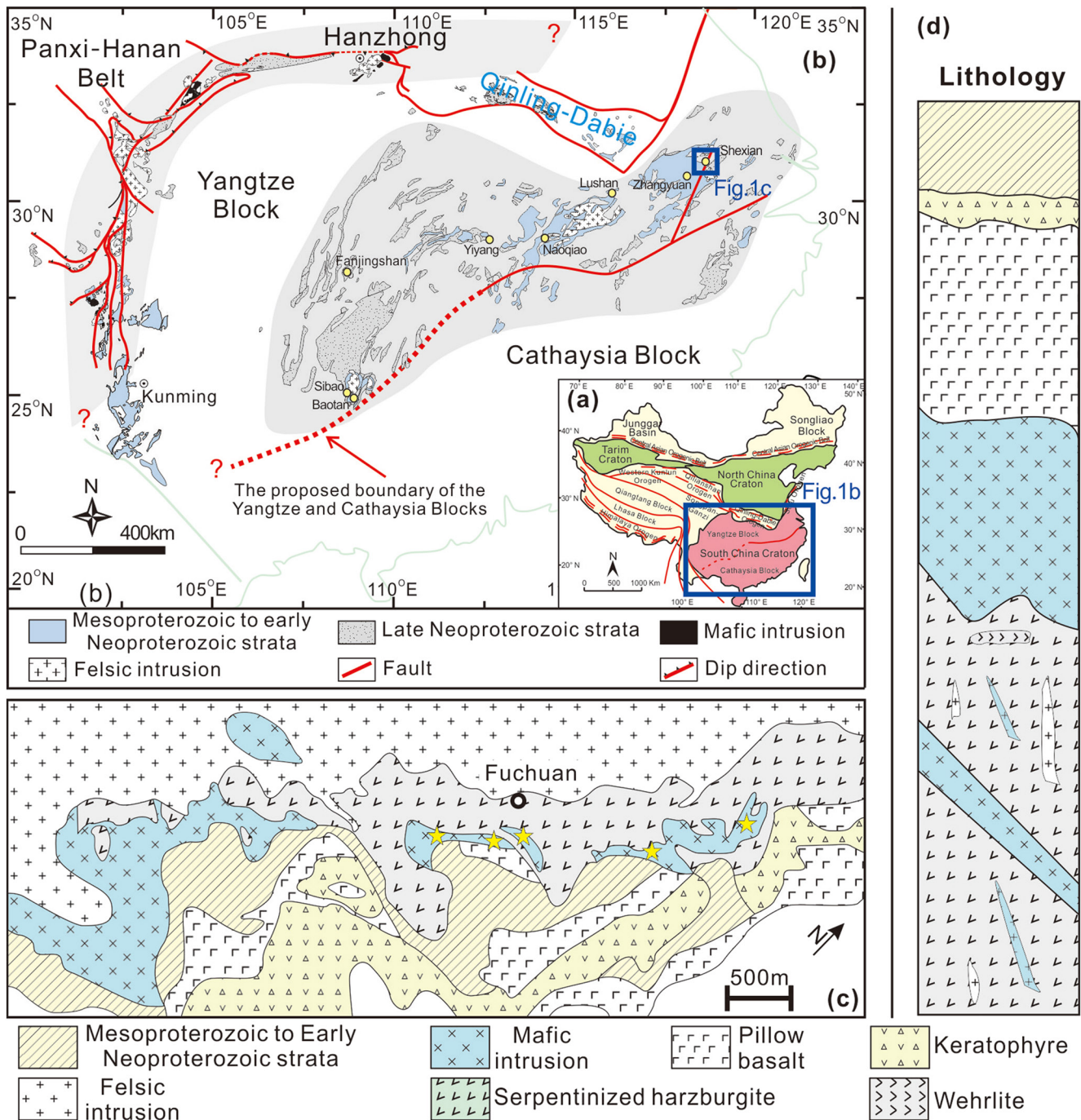
Figure 1. (a and b) Regional map showing locations of the Fuchuan ophiolite and some key Neoproterozoic igneous rocks in the Jiangnan Belt, South China (Zhao et al., 2011). Simplified geological map (c) and schematic lithology (d) of the Fuchuan ophiolite. The yellow stars indicate the sampling locations.

3. Analytical Methods

3.1. In Situ Zircon U-Pb Dating

Zircon grains were separated using standard density and magnetic procedures, and then handpicked and mounted on epoxy resin under a microscope. Cathodoluminescence (CL) images of zircon were taken using a Gatan Mono CL4 system attached to a Zeiss Sigma 300 field emission scanning electron microscope, at the State Key Laboratory of Geological Processes and Mineral Resources (GPMR), China University of
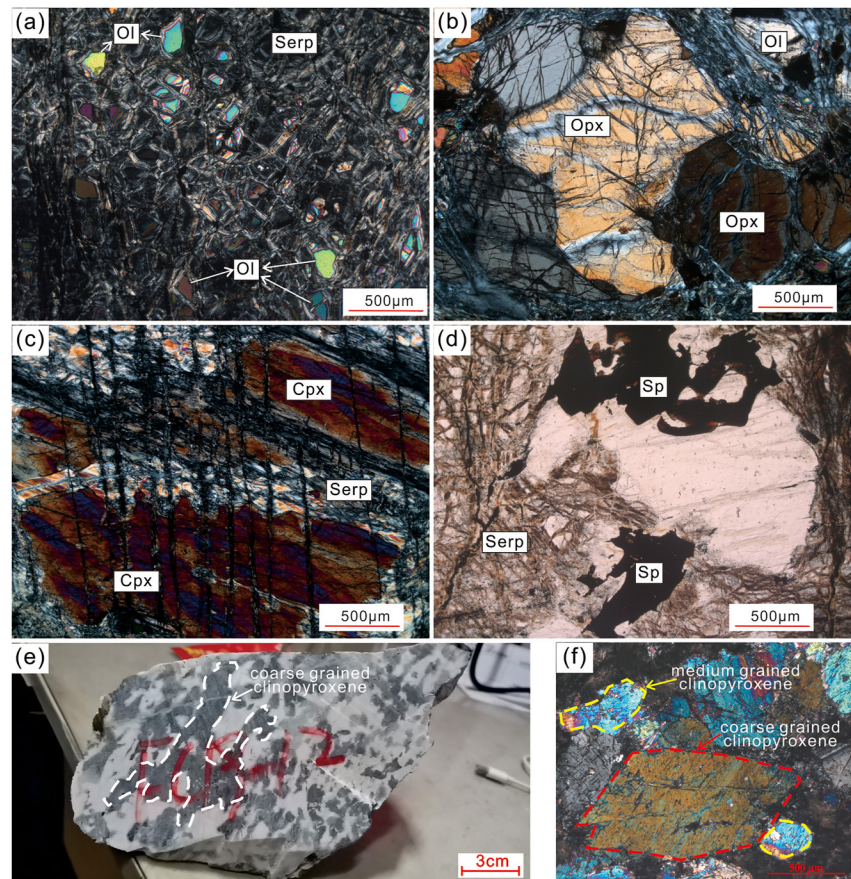
Figure 2. Hand specimen and/or microscope photos of the Fuchuan harzburgite (a–d) and cumulate gabbro (e–f). *Abbreviations:* Ol, olivine; Cpx, clinopyroxene; Opx, orthopyroxene; Sp, spinel; Serp, serpentine.

Geosciences, Wuhan. Zircon U-Pb ages were measured using a Nu Instrument MC-ICP-MS coupled to a Resonetics Resolution M-50-HR excimer laser ablation system, hosted at the University of Hong Kong. The properties of laser beam are 32 μm, 5 J cm^{-2}, and 4 Hz. Zircon 91,500 was used as an external standard to normalize isotopic discrimination and the quality of analyses was monitored by zircon GEMOC GJ-1. Raw data was reduced offline by the ICPMSDataCal procedure (Liu et al., 2008). Common lead was corrected by the EXCEL program designed by Andersen (2002). Analysis results are reported with 1σ error and presented in Table S1. Concordia diagrams, Concordia age, and weighted average age were performed using Isoplot/EX_ver3.7 (Ludwig, 2003).

3.2. Mineral Energy-Dispersive X-Ray Spectrometers (EDS) Mapping and Electron Probe Microanalyzer (EPMA) Analysis of Mineral

Compositional mapping of minerals was performed using an Oxford Instruments X-MaxN EDS system on Zeiss Sigma 300 FESEM at GPMR, under conditions of 8.5 mm working distance, 120 μm aperture size, 20 kV electronic high tension. X-ray signal intensity distribution was processed by INCA Energy Procedure to delineate the qualitative element mapping. Backscatter electron images were captured by Zeiss Sigma 300 FESEM using a high-definition backscatter electron detector to select the location for EPMA and LA-ICP-MS analyses to avoid cracks and inclusions.

Mineral oxides analyses were obtained using a JEOL JXA-8230 EPMA with four wavelength-dispersive spectrometers at the Center for Global Tectonics, School of Earth Sciences, China University of Geosciences (Wuhan). Diameter of 1 μm beam, 20 nA probe current, and 15 kV accelerating voltage was used. Dwell times were 10 s on individual element peaks and 5 s on background locations adjacent to peaks. On-line

ZAF (atomic number, absorption, and fluorescence) correction procedure was used to calculate Raw X-ray intensities. Details of Operating conditions are described in Ning et al. (2019). A series of natural standards and synthetic SPI, including Olivine for Si, Rutile for Ti, Pyrope Garnet for Fe and Al, Diopside for Ca and Mg, Sanidine for K, Jadeite for Na, Rhodonite for Mn, and Apatite for P, were utilized and changed based on the minerals being analyzed. The results are listed in Tables S2 and S3.

3.3. In Situ Clinopyroxene and Olivine Trace Elements Analysis

Trace element analyses of minerals were performed by LA-ICP-MS at Nanjing FocuMS Technology Co. Ltd. Teledyne Cetac Technologies Analyte Excite laser-ablation system (Bozeman, Montana, USA) and Agilent Technologies 7,700× quadrupole ICP-MS (Hachioji, Tokyo, Japan) were combined for the experiments. The 193 nm ArF excimer laser, homogenized by a set of beam delivery systems, was focused on mineral surface with a fluence of 6.0 J cm^{-2}. The ablation protocol employed a spot diameter of 33 μm at 6 Hz repetition rate for 40 s. Helium was used as carrier gas to efficiently transport aerosol to ICP-MS. United States Geological Survey basaltic glasses, including BIR-1G, BHVO-2G, and BCR-2G, were used as external calibration standards as these are of similar matrix as anhydrous silicate. Raw data reduction was performed offline by ICPMSDataCal software (Liu et al., 2008) and the results are presented in Tables S4 and S5. Chinese Geological Standard Glasses CGSG-5, ML3B, GOR128-G, and GOR132-G were treated as unknown samples to monitor the quality of data (Table S6; Hu et al., 2011).

4. Sampling and Results

4.1. Zircon U-Pb Dating

Zircon grains from two cumulate gabbro samples are colorless and show either clear oscillatory zoning or a homogeneous texture, with high Th/U ratios ranging from 0.34 to 1.15, indicative of a magmatic origin. Four zircon grains yield older U-Pb ages (868–946 Ma) than the main age population and may represent xenocrysts from subducted slab sediments, cf. xenocrysts in the oceanic Cretaceous Caribbean island-arc (Torró et al., 2018). Sample FC10–11 contains five younger zircon grains with U-Pb ages from 653 to 808 Ma, which we ascribe to lead loss due to its high U contents (206–687 ppm; Table S1). Three discordant ages from sample FC10–11 were also excluded in the following calculation and discussion. Weighted mean $^{206}Pb/^{238}U$ ages calculated from concordant analyses are 845 $\pm$ 3 Ma (2σ, MSWD = 1.0, n = 23) for samples FC10–11 and 848 $\pm$ 3 Ma for sample FC10–33 (2σ, MSWD = 0.74, n = 29; Figure 3). Statistically, both the fine-grained and cumulate gabbro shows a single population crystallization age, that is consistent with previous U-Pb zircon dating on the gabbro and plagiogranite intrusions in the Fuchuan ophiolite (850–830 Ma; Li & Zhao, 2020; Shu et al., 2019; Zhang et al., 2012; C. L. Zhang et al., 2013).

4.2. Geochemistry of Olivine, Orthopyroxene, and Chrome Spinel From the Fuchuan Harzburgite

Individual olivine and spinel grains are homogeneous in composition (Figures 4a and 4b). Olivine grains from the Fuchuan harzburgite have high MgO (48.8–51.2 wt.%) and low FeO^T (7.3–8.2 wt.%) with relatively constant forsterite (Fo = molar 100 × Mg/(Mg + Fe)) values ranging from 91.6 to 92.2. Olivine analyses show high NiO (0.21–0.30 wt.%), low Cr$_2$O$_3$ (<0.077 wt.%), Al$_2$O$_3$ (<0.029 wt.%), TiO$_2$ (<0.034 wt.%), MnO (0.04–0.09 wt.%), and variable CaO (0.007–0.069 wt.%) contents (Table S2). Orthopyroxene grains from the Fuchuan harzburgite have a restricted range of MgO (31.6–35.9 wt.%) and FeO^T (4.4–5.6 wt.%) with low CaO (0.1–2.6 wt.%) contents. The orthopyroxene has Mg# values that vary from 89.4 to 94.5, with an average of 91.2 (Table S2). Spinel grains from the Fuchuan harzburgite have high Cr$_2$O$_3$ (39.9–50.1 wt.%) and low Al$_2$O$_3$ (20.5–28.5 wt.%) contents (Table S2). They show significantly higher Cr# (48.5–62.1; Cr# = molar Cr/(Cr + Al) × 100) and lower Mg# (44.3–60.1; Mg# = molar Mg^{2+}/(Mg^{2+} + Fe^{2+}) × 100) values than those of abyssal peridotite, and are akin to forearc peridotite (Figure 5).
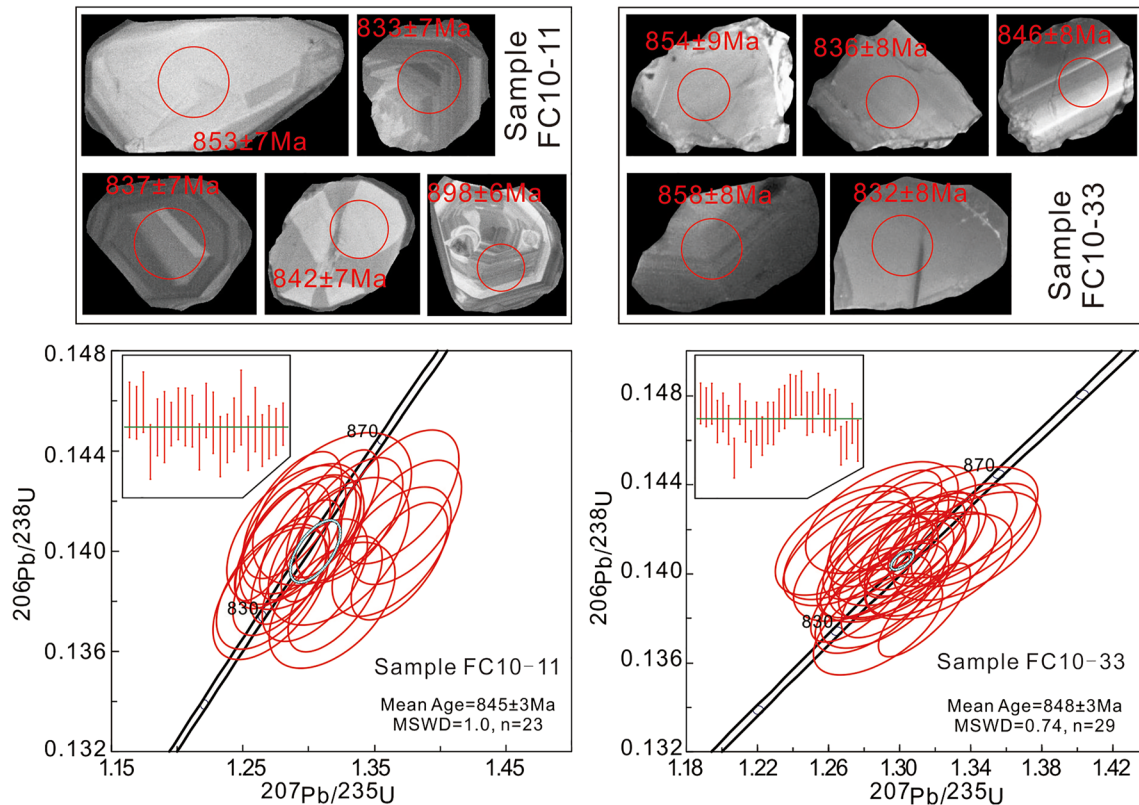
Figure 3. Cathodoluminescence (CL) images of zircons and U-Pb Concordia diagrams for the cumulate gabbro of the Fuchuan ophiolite. The diameter of red circles in the CL images is 33 μm. Analytical errors are shown at the 2σ level.

4.3. Major and Trace Elements of Clinopyroxene From Cumulate Gabbro

Clinopyroxene grains from the cumulate gabbro are mainly black and occasionally gray (Figure 2e), and range in composition from augite to diopside with homogeneous geochemical compositions (Figure 4c). Two groups of clinopyroxene can be identified based on their petrographic and geochemical characteristics. (a) Coarse grained clinopyroxenes (>1 mm) that have a tabular, euhedral shape with high FeO^T contents (4.3–9.2 wt.%) and low Mg# values (74.1–86.6); (b) Medium grained clinopyroxenes (<1 mm) that are anhedral with low FeO^T contents (0.9–3.9 wt.%) and high Mg# values (88.4–97.3; Figures 6a and 6b and Table S3). Using a Fe-Mg equilibrium exchange coefficient between clinopyroxene and melt of 0.28 ± 0.08 (Putirka, 2008), the corresponding Mg# of equilibrium melts with the coarse and medium grained clinopyroxene are extremely high ranging from 48.4 to 64.4 and 67.6 to 90.9, respectively. This Fe-Mg equilibrium exchange coefficient is derived from a normal distribution with calculated exchange coefficients ranging from 0.04 to 0.68 (this range is based on 1,245 experimental observations on Fe-Mg equilibrium exchange coefficients). In addition, the Fe-Mg equilibrium exchange coefficient is generally controlled by melt compositions, temperature, pressure and oxygen fugacity (Putirka, 2008). Therefore, in order to demonstrate the effect of using a lower Fe-Mg exchange coefficient we have used a value of 0.2 as the Fe-Mg equilibrium exchange coefficient to calculate melt Mg#. Using 0.2 as an equilibrium exchange coefficient yields Mg# in the equilibrium melts of 36.4–56.3 and 59.9–87.7 (most values <82), in the coarse and medium grained clinopyroxene, respectively.

The coarse grained clinopyroxenes have markedly depleted light REE and flat middle-heavy chondrite-normalized REE patterns, whereas the medium grained clinopyroxenes, while also depleted in the LREE show a gradual increase from La through the middle REE to Lu (Figure 7). On primitive mantle normalized diagrams (Figure 8), the coarse grained clinopyroxenes have higher REE and HFSE contents and lower Th and U contents than the medium grains. These medium grained clinopyroxenes have more significant negative Zr-Hf anomalies than the coarse grained clinopyroxenes (Figure 8).
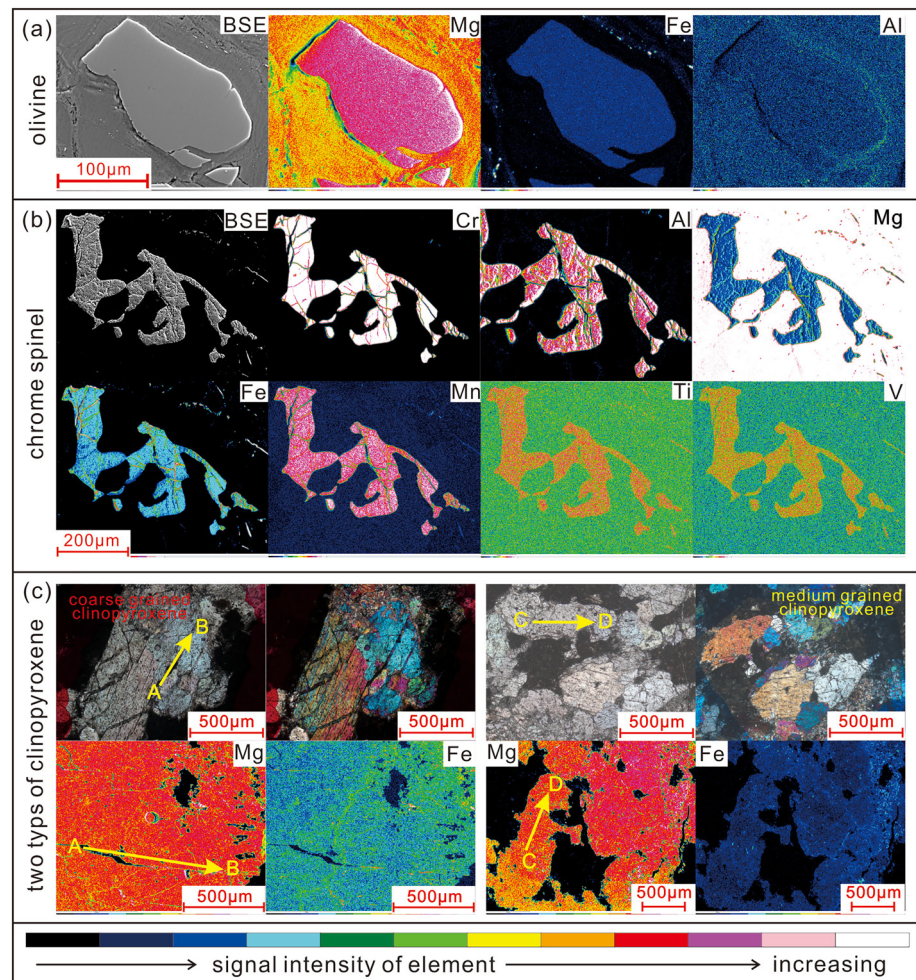
Figure 4. Mapping of individual olivine (a) and spinel (b) grains from the Fuchuan harzburgite. Mapping of clinopyroxene (c) from the cumulate gabbro. Arrows A → B and C → D indicate the consistent direction of mineral morphology in images. The signal intensity of elements for mapping is shown at the bottom.

5. Discussion

5.1. Signatures in the Fuchuan Harzburgite: Forearc Setting Indications

Extensive serpentinization of the Fuchuan harzburgite means that it is difficult to identify the original lithology and mineralogy of the rock. However, high Sc (2.4–5.1 ppm) and Mn (970–1,062 ppm) along with low Zr (<4.9 ppb) and highly variable Al contents (5.5–48.1 ppm) in olivine from the Fuchuan harzburgite (Table S5) indicate a spinel harzburgite affinity (De Hoog et al., 2010). Moreover, olivine grains with Fo values higher than 92.0 have Ni contents (3,022–3,289 ppm; average of 3,147 ppm) higher than olivine from garnet peridotite (~3,000 ppm; De Hoog et al., 2010). This also suggests that the original lithology was spinel harzburgite. Although the spinel grains in the Fuchuan harzburgite are xenomorphic, they have similar $Cr\#_{spinel}$-$Mg\#_{spinel}$ to spinel from depleted mantle peridotite (Dare et al., 2009), suggesting that they are not affected by sub-solidus alteration and represent residues after melting and melt extraction. In addition, the Cr# and Mg# values of spinel in the Fuchuan harzburgite are lower than those found in boninites and are similar to spinel from forearc ophiolites (Figure 5), such as the Bakedong ophiolite (Kim et al., 2011), indicating a forearc setting affinity.

To estimate the temperature recorded by the Fuchuan harzburgite, pressures of 1.0, 1.5, and 2.0 GPa (stability field of spinel) were used in the calculation of the olivine-spinel Mg-Fe^{2+} exchange thermometer (T_{B91}) and Ca-in-orthopyroxene thermometer (T_{BKCa90}; Ballhaus et al., 1991; Brey & Köhler, 1990; O'Neill &
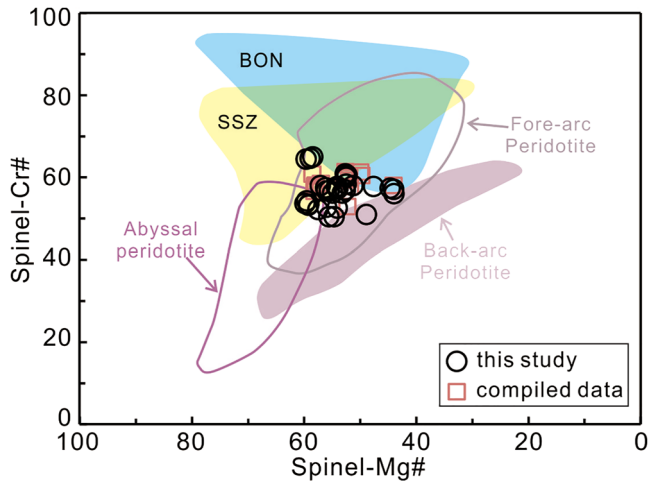
Figure 5. Plot of spinel Cr# versus Mg# (modified from Dick and Bullen [1984], Kim et al. [2011], and C. L. Zhang et al. [2013]). The compiled data are average compositions for each sample and are from Ding et al. (2008) and Y. Zhang et al. (2013).

Wall, 1987). These pressures are based on the absence of fresh grains and/or altered imprint for plagioclase and garnet in the Fuchuan harzburgite (Bernstein et al., 1998). Calculations using T_{B91} with an olivine Fo value of 92.0 indicate that the temperature ranges from 667 to 814°C (average of 737°C), 730 to 886°C (average of 807°C), and 793 to 959°C (average of 877°C) for 1.0, 1.5, and 2.0 GPa, respectively. Temperatures calculated based on the Ca contents of orthopyroxene (T_{BKCa90}; Brey & Köhler, 1990) range from 978 to 1,185°C (1,097°C), 1,003–1,214°C (1,124°C), and 1,027–1,243°C (1,151°C) for 1.0, 1.5, and 2.0 GPa, respectively, with confidence range of ±38°C (2σ; with exception of 624–640°C for sample FC10–55). Calculations using the Al in olivine (Fo = 92.0) and spinel geothermometer are nearly constant from 984 to 1,009°C (T_{C14}, average of 993°C) with uncertainties of ±60°C (Coogan et al., 2014; Wan et al., 2008). The Al-Cr exchange geothermometer in orthopyroxene also yields a high temperature (T_{WS91}:1,063–1,211°C, average of 1,145°C) with confidence range of ±32°C (2σ), except for sample FC10–55 (699–720°C; Witt-Eickschen & Seck, 1991). Low temperatures recorded in the orthopyroxene of sample FC10–55 may be the result of late-stage re-equilibration with calcium and aluminum, considering its lower CaO and Al_2O_3 contents relative to other samples. Even using a pressure of 2.0 GPa, T_{B91} shows obviously lower temperature than T_{C14} and T_{WS91}, suggesting that the main controller of olivine-spinel Fe-Mg exchange temperatures is not pressure. An alternative interpretation is that the temperature would go down during the uplift and exhumation processes of the Fuchuan harzburgite and therefore, the olivine-spinel Fe-Mg exchange geothermometer would record decreased temperatures due to significantly rapid exchange equilibrium of Mg and Fe between olivine and spinel (Ballhaus et al., 1991). Therefore, the Fuchuan harzburgite records a relatively high temperature process (1,000–1,200°C $\pm$ 60°C; T_{BKCa90}, T_{C14}, and T_{WS91}).
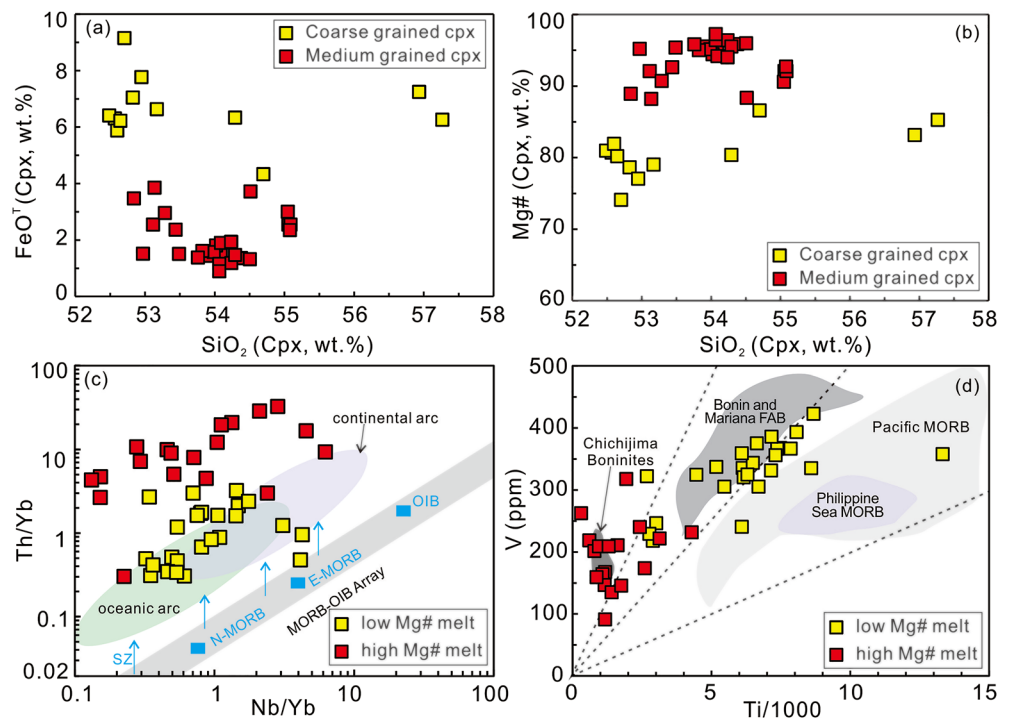
Figure 6. FeO^T and Mg# versus SiO$_2$ (a and b) of clinopyroxene from the cumulate gabbro. Nb/Yb versus Th/Yb (c) and Ti/1,000 versus V (d) of melt composition equilibrium with two types of clinopyroxenes. The colored areas are modified from Ishizuka et al. (2014).
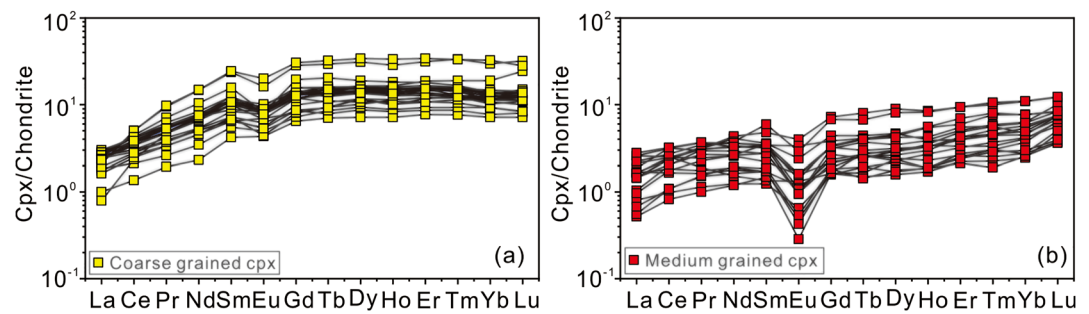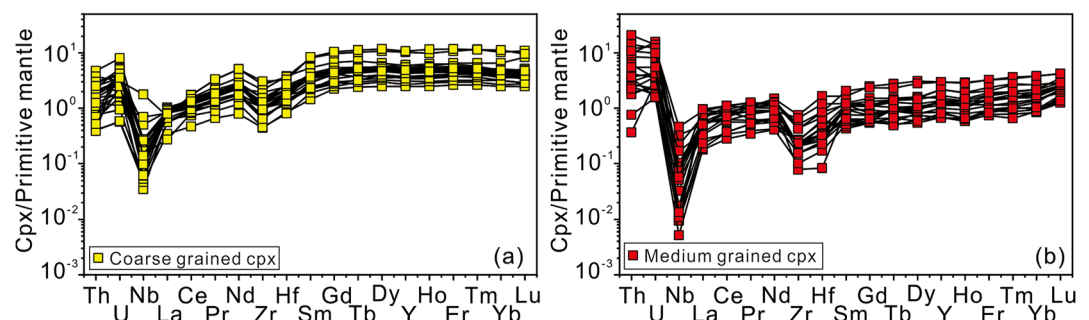
Figure 7. Chondrite normalized REE patterns for coarse and medium grained clinopyroxene. Normalization data are from Sun and Mcdonough (1989).

Calculation of the degree of partial melting based on Cr# values of spinel (Hellebrand et al., 2001) suggests that the Fuchuan harzburgite represents a mantle residue after 17%–19% melting and melt extraction from the depleted mantle (DM). Alternatively, the degree of partial melting can also be calculated from olivine compositions using the equation of $F_{melting}(\%) = 14.5 \times \ln(Cr\#^{ol}) + 26$ (De Hoog et al., 2010), indicate an extent of melting ranging from 18% to 23% of DM, with Cr#^{ol} varying from 0.60 to 0.82 for the Fuchuan harzburgite. The analyzed orthopyroxenes from the Fuchuan harzburgite with high variation of Al_2O_3/MgO ratios (0.01–0.07) also indicate a relative high degree of melt depletion (Zhou et al., 2021). Although the harzburgites have been strongly serpentinized, work by Li and Zhao (2020) has shown that the serpentinization did not significantly alter the original whole-rock geochemical compositions. Modeling of fractional melting under adiabatic decompression conditions suggests that the Fuchuan harzburgites are likely residues after ∼20%–25% melt extraction of the primitive mantle (Figure 9). However, the Fuchuan harzburgite samples fall mostly outside of the fields for melting primitive mantle, such as low Al_2O_3, TiO_2, and higher SiO_2 contents (Figures 9b–9d), and suggest that the original mantle must have been depleted by previous melt extraction. The high olivine Fo values and absence of clinopyroxene in the Fuchuan harzburgite indicate complete melting of clinopyroxene, which is consistent with experimental results of ∼20% partial melting of spinel peridotite (Herzberg, 1992; Hirose & Kushiro, 1993).

Based on the above discussion on the low pressure, high temperature, high degree of melt extraction, the Fuchuan harzburgite may represent a fossil remnant of forearc lithospheric mantle.

5.2. Geochemical Fingerprints of Forearc Basalt and Boninite in the Fuchuan Ophiolite

The two groups of clinopyroxene identified in the Fuchuan gabbro may be the result of magma evolution through crystal fractionation or accumulation. However, such a relationship is implausible for various reasons: (a) medium grained clinopyroxenes (high Mg#) are more anhedral than, and occasionally surround, coarse grained clinopyroxenes (Figure 2f), indicating that medium grained clinopyroxenes (high Mg#) were formed later; (b) medium grained clinopyroxenes have higher Ba, Th, and U contents and lower HFSE

Figure 8. N-MORB normalized multi-element diagrams for coarse and medium grained clinopyroxene. Normalization data are from Sun and Mcdonough (1989).
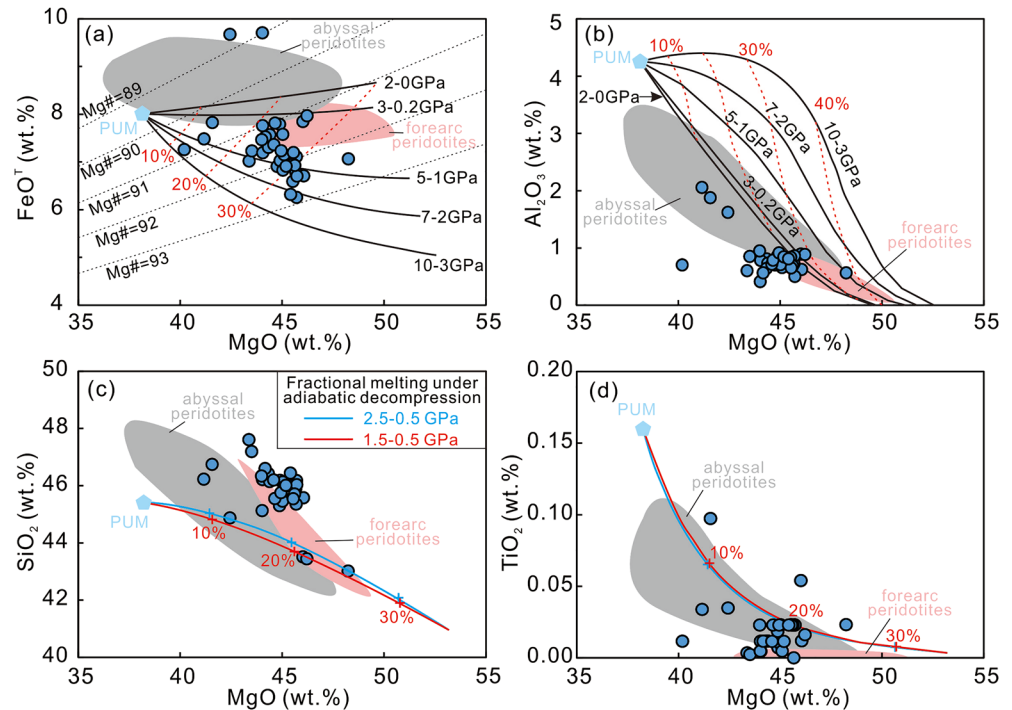
Figure 9. Whole-rock FeO^T, Al$_2$O$_3$, SiO$_2$, and TiO$_2$ versus MgO variations of the Fuchuan peridotite (modified from Xiong et al. [2017] and data compiled from Li and Zhao [2020]). The compiled whole-rock major oxides have been normalized to 100% without volatile compositions. (a and b) The solid black curves represent the modeled compositional contours of residual peridotites, using the method of Herzberg (2004); the pressures near the solid black curves indicate the starting and final pressures of the fractional melting under adiabatic decompression conditions; the red-dashed lines mark degrees of melt extraction (10%, 20%, and 30%). The black dashed lines represent the evolution of Mg# ranging from 89 to 93. (c and d) The blue and red solid curves represent the compositional contours of the residual peridotites after decompression fractional melting at 2.5–0.5 and 1.5–0.5 GPa, respectively, using the approach of Niu (2004). The crosses indicate the melting extents (f) of 10%, 20%, and 30%. The primitive upper mantle, abyssal, and forearc peridotite compositions are from Xiong et al. (2017).

(e.g., Zr and Hf) and REE contents than those of coarse grained clinopyroxenes (Figure 8), rather than increasing concentrations of these incompatible elements from high Mg# to low Mg# clinopyroxene; (c) the more marked depletion of heavy REE in medium grained clinopyroxenes ([Gd/Lu]$_N$ = 0.26 to 0.66 with the majority <0.6) than coarse grained clinopyroxenes ([Gd/Lu]$_N$ = 0.64–1.19 with the majority >0.7; Figure 8) also indicate two episodes of melt extraction, because fractional crystallization of olivine and orthopyroxene cannot modify the REE patterns (McDade et al., 2003a). Therefore, two types of clinopyroxene may have been derived from different melts extracted from mantle sources.

To calculate the trace element compositions of melt that was in equilibrium with clinopyroxene, hydrous mineral/melt partition coefficients (Table S7; McDade et al., 2003a, 2003b) and compositions of clinopyroxene were used. Calculated melts (low Mg#) in equilibrium with the coarse grained clinopyroxene have N-MORB-type REE patterns and are enriched in LILE (e.g., Ba and U) and depleted in HFSE (e.g., Zr and Hf) relative to N-MORB (Figure 10a), and so resemble forearc basalts from the Oman ophiolite and the Zedang ophiolite in South Tibet, and the Deep-Sea Drilling Project (DSDP) sites 458 and 459 and International Ocean Discovery Program Expedition 352 sites U1440 and U1441 in the IBM forearc (Goodenough et al., 2014; Reagan et al., 2010; Shervais et al., 2019, 2021; Xiong et al., 2016). The clinopyroxene-plagioclase mineral assemblages of the cumulate gabbro from the Fuchuan ophiolite are remarkably similar to the mineralogy of the IBM forearc gabbro (clinopyroxene + plagioclase + minor magnetite), which probably crystallized after early olivine fractionation from the primitive forearc basalt (Reagan et al., 2017, 2019). In addition to this, some medium-to-fine-grained gabbro intrusions in the Fuchuan ophiolite have N-MORB-like chondrite-normalized REE patterns and are enriched in LILE (e.g., K, U, and Cs; Shu et al., 2019; Zhang et al., 2012), which provides petrological evidence of forearc basaltic magmas.
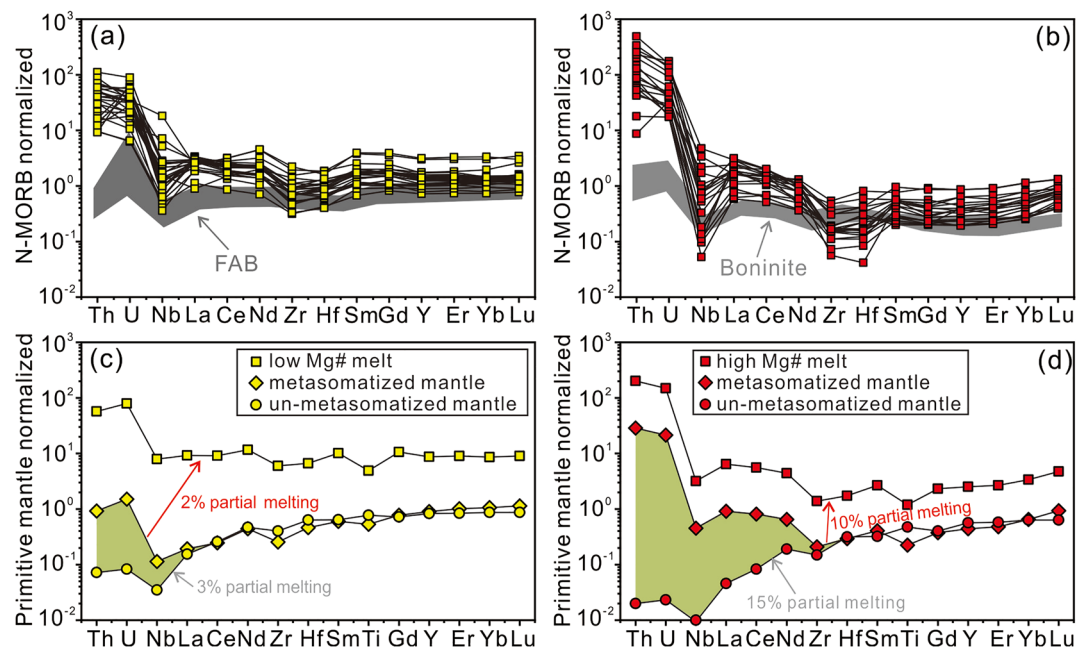
Figure 10. (a and b) N-MORB normalized multi-element diagrams of melt equilibrium with the coarse and medium grained clinopyroxene. Forearc basalt and boninite data are from Reagan et al. (2010) and Woelki et al. (2018). (c and d) Primitive mantle-normalized incompatible trace element patterns for melt equilibrium with the average clinopyroxene compositions, calculated metasomatized mantle, and modeled pre-subduction mantle. The degree of depletion of the pre-subduction mantle is given in weight percent (f) in gray text. Partial melts were produced by the metasomatized mantle, and the degree of partial melting is shown by red fonts. The shaded area in panel (c and d) indicates the contribution of elements carried by aqueous fluid/melt to mantle source. Normalization data are from Sun and Mcdonough (1989). Bulk partition coefficients are from McDade et al. (2003a, 2003b) and https://kdd.earthref.org/KdD/ and the primitive mantle composition of Sun and Mcdonough (1989) were used to calculate the degree of mantle wedge depletion.

Significantly, the melts in equilibrium with the medium grained clinopyroxene show U-shaped REE patterns and are more enriched in LILE than the low Mg# melt (Figure 10b). These geochemical signatures, combined with their high Mg#, suggest that the medium grained clinopyroxene may originate from a boninite-like melt (Pearce & Arculus, 2021; Shervais et al., 2021). Calculation also shows that high Mg# melts have extremely low TiO_2 contents (0.2–0.7 wt.%, average of 0.26 wt.%), consistent with typical boninite (Pearce & Arculus, 2021; Pearce & Reagan, 2019). The negative Zr-Hf anomaly in these melts (Figure 10b) may indicate that Zr and Hf were retained by accessory mineral phases in the residue (e.g., zircon) during melting of subducted sediment (Schwindinger et al., 2020). High-Si boninitic melts are enriched in Si and Mg, therefore, it would be expected that orthopyroxene and olivine would crystallize in preference to clinopyroxene (Pearce & Arculus, 2021). However, there is no olivine and orthopyroxene in the studied gabbro, indicating that these infiltrating melts are similar to low-Si boninite (Pearce & Reagan, 2019). It should be noted that low-Si boninite can occur near trench sea-floor rifting (back-arc basin), such as the West Mata volcano in the Northeast Lau Basin, and these boninitic magmas have low SiO_2 and high CaO contents, accompanied by abundant volatiles from the subducting slab (Falloon et al., 2007; Resing et al., 2011). However, Zhao and Asimow (2014) suggest that some pillow lavas from the Fuchuan ophiolite show affinity with high-Si boninite, and these lavas have high SiO_2 (up to 60.5 wt.%) and low CaO (<8 wt.%) contents (normalized to volatile-free), contrasting with the back-arc basin boninites (Falloon et al., 2007; Resing et al., 2011). A previous study reported low Al_2O_3 (0.51–0.95 wt.%) and high MgO (44.0–48.2 wt.%) contents of the Fuchuan harzburgite (Li & Zhao, 2020), similar to forearc peridotite rather than back-arc peridotite, which is consistent with the spinel Cr#-Mg# values of this study (Figure 5). Low TiO_2/Yb ratios (0.03–0.39, lower than a typical OIB value of 2.9) and $[Sm/Yb]_N$ (0.47–1.40) values of the calculated melt composition, also indicate shallow melting, a feature consistent with forearc basalt and boninite generation.

Physical conditions calculated for the Fuchuan harzburgite, including high temperature (1,000–1,200°C), low pressure (stability field of spinel), a high degree of melt extraction (17%–23%), and a hydrous source, also indicate a forearc setting, where the formation of forearc basalt and boninite is very likely. In addition, Ti/V ratios of the calculated high Mg# and low Mg# melts show boninite and forearc basalt features, respectively (Figure 6). Although vanadium in clinopyroxene depends strongly on the oxygen fugacity of the magma, the low Ti contents of the high Mg# melts still indicate a boninite affinity. Therefore, the Fuchuan ophiolite is more likely to have formed during the initiation of subduction rather than from near-trench rifting.

An approach similar to König et al. (2010) can be used to determine the contribution of slab/sediment-derived components to the mantle source of the Fuchuan high and low Mg# melts. The incompatible element compositions of metasomatized mantle wedge are modeled by modal batch melting using bulk partition coefficients (Table S7) and average melt composition. The incompatible element compositions of un-metasomatized mantle wedge were modeled by non-modal batch melting using primitive mantle. The modal of harzburgite is composed of 71% olivine, 23% orthopyroxene, 3% clinopyroxene, and 3% spinel (König et al., 2010). Non-modal batch melting depends on hydrous reaction of lherzolite: 0.82 cpx + 0.40 opx + 0.08 sp = 0.30 ol + 1.0 melt (König et al., 2010). Modeling results indicate that the low Mg# melts were derived from a slightly depleted lherzolite mantle source (with 3% melt extraction), which was metasomatized mainly by LILE-enriched aqueous fluids with minor or no slab melt (Figure 10c). Although field evidence suggests that slightly depleted lherzolite does not occur in the Fuchuan ophiolite, it should be noted that it is similarly absent from the IBM. The evidence from these low Mg# melts does indicate their existence during the early stage slab subduction, confirming the original intactness of mantle section for the Fuchuan ophiolite. In contrast, the high Mg# melts were derived from a highly depleted mantle source (with 15% melt extraction), which was modified by both aqueous fluids and slab melts (LILE, LREE, and HFSE) (Figure 10d). These results are consistent with the high degree (17%–19%) of melt extraction recorded in Cr-spinel from Fuchuan harzburgite. Therefore, we conclude that the low Mg# clinopyroxene crystallized from forearc basalt melt and accumulated in the magma chamber, which was then infiltrated by later high Mg# boninitic-like melt. A similar sequence of magma evolution is also identified in the compositional variation of clinopyroxenes from the cumulate rocks in the Ordovician Bay of Islands ophiolite in Newfoundland (Suhr et al., 1998) and from the gabbroic sequence in the Oman ophiolite (Yamasaki et al., 2006).

5.3. A Neoproterozoic IBM-Like Subduction System in South China

Based on data from this study and from published work on harzburgite and arc-related calc-alkaline pillow lavas (Li & Zhao, 2020; Yang et al., 2021; Zhang et al., 2012; C. L. Zhang et al., 2013; Zhao & Asimow, 2014), it is clear that the Fuchuan ophiolite has the following features: (a) high degree of melt extraction of the mantle section; (b) high temperature and low pressure of magma extraction recorded in its mantle peridotite; (c) preserved fluid/melt-metasomatized trace element signatures in clinopyroxene and mantle peridotite; (d) magma generation that evolves from forearc basalt to boninite to mature arc-related calc-alkaline lava; (e) occurrence of podiform chromitites within the harzburgite; (f) coeval granite intruded into the mantle section of the Fuchuan ophiolite has high zircon $\delta^{18}O$ values (up to 11‰; our unpublished data). All these features strongly suggest that the Fuchuan ophiolite was formed in a forearc setting, and record slab subduction stages from initiation to mature arc (Figure 11).

Geological and geophysical studies reveal that the IBM forearc oceanic crust generated in the initial stages of subduction is similar to the setting in which many ophiolites formed in the geological record (Ishizuka et al., 2014). It has been proposed that the magmatic evolution of IBM forearc oceanic crust starts with initial forearc basalts, that progress to boninites and island arc tholeiites, and to finally calc-alkaline lavas (Reagan et al., 2010; Shervais et al., 2019; Woelki et al., 2018). The similarity of stratigraphic sequences in the Fuchuan ophiolite to IBM forearc oceanic crust (Figure 12) supports the existence of a Neoproterozoic (ca. 850 Ma) IBM-like subduction system on the southeastern margin of the Yangtze Block.

The geochemical signatures of some sporadic intrusive and extrusive rocks (860–825 Ma) from the southeastern margin of the Yangtze block also support this conclusion (Li & Zhao, 2020; Shi et al., 2020; Tian et al., 2020, 2021; Yao et al., 2019): (a) ca. 860–840 Ma basalt and dolerite with N-MORB geochemistry are enriched in LILE (e.g. Th, U, and Ba) and are thus more akin to forearc rather than back-arc basalt (Y. Wang
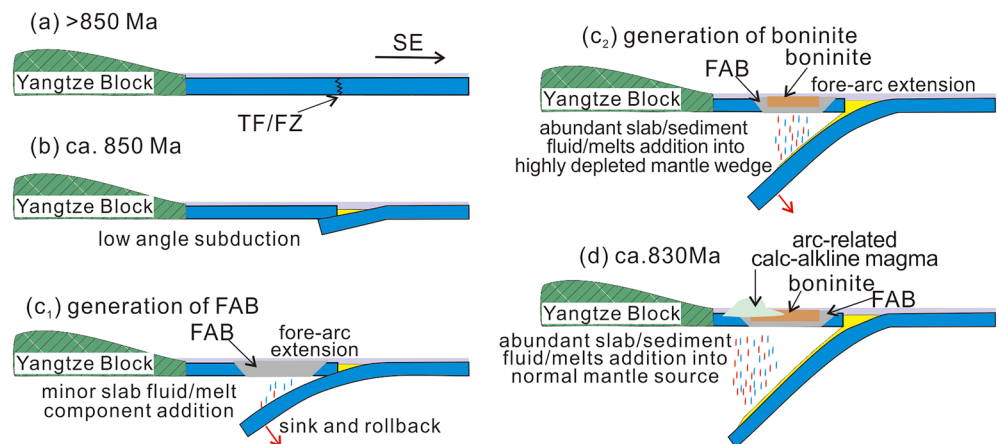
Figure 11. Schematic diagram of subduction initiation, formation of the forearc, and magmatic evolution of the subduction system, modified after Stern et al. (2012) and Li et al. (2019). (a) A hypothetical transform fault or fracture zone (TF/FZ), located at the southeast margin of the Yangtze Block. (b) Sinking of older, thicker, colder, and denser oceanic lithosphere below young, thinner, hotter, and more buoyant lithosphere along the TF/FZ with a low angle ($<30°$); (c_1) when the depth of subduction slab is sufficient to transform to eclogite facies, sinking and rollback of the slab results in extension of the overlying plate and generation of forearc basalt with no or little subduction aqueous fluid/melt; (c_2) with further sinking, the slab is heated up to melting temperatures while at relatively shallow depth, and these slab melts then interact with residual depleted mantle to produce boninite. (d) Further downward movement of the slab triggers the formation of calc-alkaline island arc magmas. Due to a shorter time for the formation of forearc basalt and boninite in IBM, the precise time in cartoon (c_1) and (c_2) for forearc basalt and boninite in the Fuchuan ophiolite is difficult. Zircon U-Pb dating suggests that they were formed at ca. 845 Ma.

et al., 2019; Yao et al., 2014; Y. Zhang et al., 2013); (b) some high-Mg basalts show high SiO_2 and MgO, low TiO_2 contents, suggesting a boninite affinity (Zhao & Asimow, 2014; Zhao & Zhou, 2013); (c) some ca. 825 Ma calc-alkaline high-Mg andesites and diorites resemble the ~14 Ma Setouchi high-Mg andesites from SW Japan (Chen et al., 2014; Tang et al., 2020; Tian et al., 2020).

5.4. Modern-Style Subduction in the Neoproterozoic

In addition to the Fuchuan ophiolite, global Neoproterozoic forearc ophiolite with relatively complete sequences, reviewed below, have been shown by the geochemistry of their mantle sequences and crustal volcanic rocks, to be similar to modern-day forearc ophiolites, such as that represented by the IBM (Figure 12). Although the geochemistry of the crustal section of the ca. 838 Ma Bir Umq ophiolite (Arabian Shield) has not yet been studied in detail (Figure 12), highly depleted mantle harzburgite ($Cr\#_{spinel}$ = 60–71) suggests a forearc setting (Abuamarah, 2020). Furnes et al. (2014) proposed that about 85% of Precambrian ophiolites with MORB signatures are linked to back-arc processes. However, these ophiolites exhibit broadly similar characteristics to the "back-arc knolls zone" of the IBM arc, such as ca. 800 Ma Shishkhid ophiolite in northern Mongolia (Kuzmichev et al., 2005) and ca. 808 Ma Onib ophiolite on the Arabian-Nubian Shield (Hussein et al., 2004).

Statistical analyses suggest that the amount of Neoproterozoic ophiolite increases significantly from ca. 850 Ma, and only a few ophiolite suites with incomplete rock sequences, including the Dunzhugur ophiolite (Siberia; Khain et al., 2002), Jiangxi and Miaowan ophiolite (South China; Li & Zhao, 2020; Peng et al., 2012), and Phulad ophiolite (NW India; Volpe & Macdougall, 1990), were dated at ca. 970–1,020 Ma (Figure 13a). These observations, combined with the abundant ophiolite fragments (<850 Ma) (Figures 13a and 13c), suggest that IBM-like subduction systems may have successfully operated since at least the latest Neoproterozoic (ca. 1,000 Ma) and may be pervasive on Earth from ca. 850 Ma. Several ophiolite suites dated at ca. 1.8–2.0 Ga (Figure 13a), such as the Purtuniq ophiolite in Canada (Scott et al., 1992), the Jormua ophiolite in Northeastern Finland (Peltonen et al., 1996), and the Flin Flon ophiolite (Stern et al., 1995; Wyman, 1999), may indicate a period of short-lived plate tectonics. However, this episode of plate tectonics was terminated by the assemblage of Nuna/Columbia supercontinent and then the Earth entered a protracted
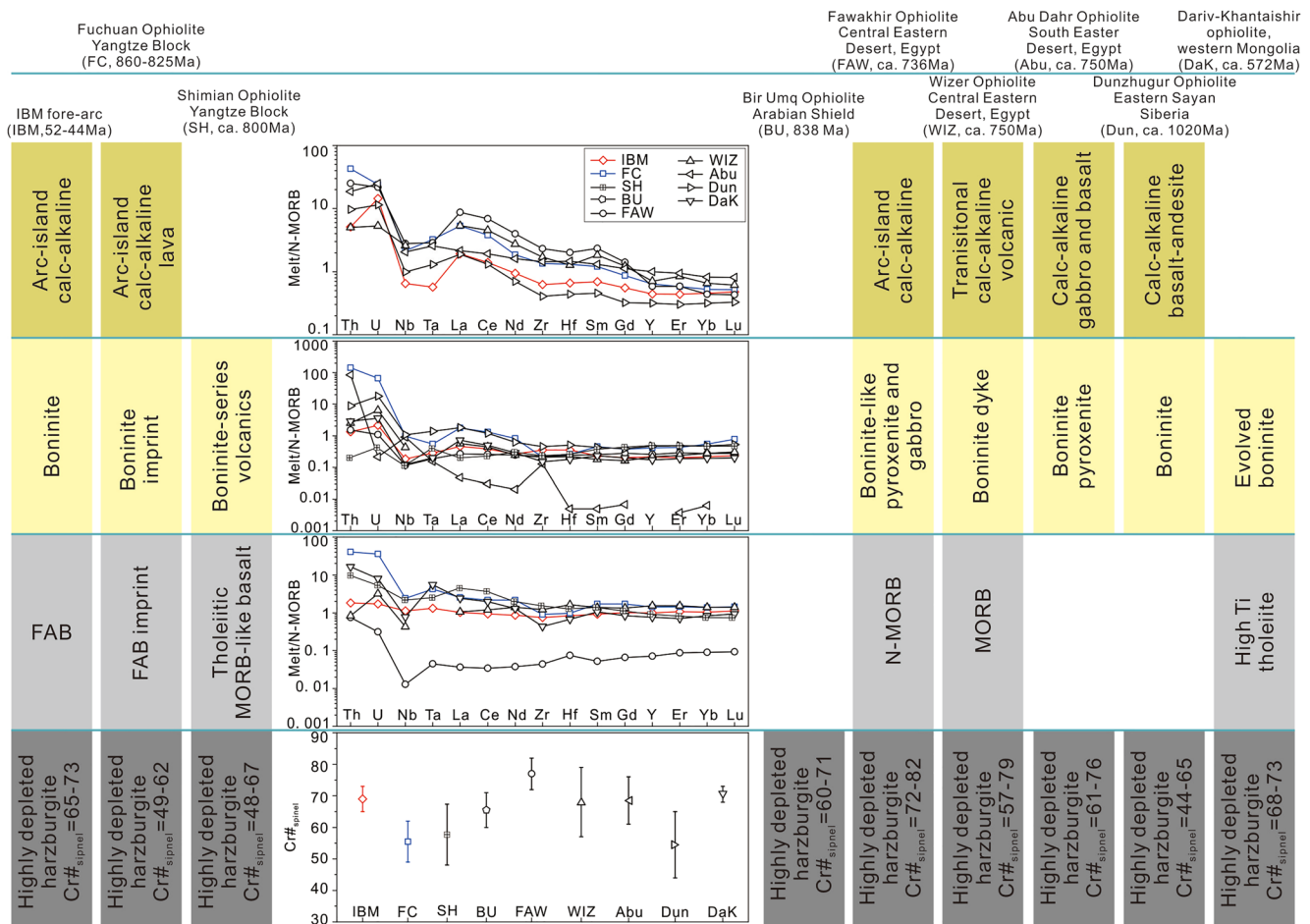
Figure 12. Neoproterozoic forearc ophiolite stratigraphic succession, Cr# values of spinel from harzburgite, and whole-rock trace element composition of the crustal section are strikingly similar to IBM forearc rock assemblages. Geochemical stratigraphy of the studied and complied ophiolites reflect the transition from an initial extension of the overlying plate through the commencement of fluid and melt release from the subducting slab, to a finally mature subduction system. The data from the IBM forearc rock assemblages, Fuchuan ophiolite (FC, this study), Shimian ophiolite (SH), Bir Umq ophiolite (BU), Fawakhir ophiolite (FAW), Wizer ophiolite (WIZ), Abu Dahr ophiolite (Abu), Dunzhugur ophiolite (Dun), and Dariv-Khantaishir ophiolite (DaK) are compiled from Abdel Halim et al. (2020), Abdel-Karim et al. (2018), Abuamarah (2020), Dandar et al. (2019), Dijkstra et al. (2006), El-Rahman et al. (2009), Farahat (2010), Farahat et al. (2011), Gahlan et al. (2015), Ishizuka et al. (2006), Morishita et al. (2011), Reagan et al. (2010), Sklyarov et al. (2016), W. Wang et al. (2017), and Zhao et al. (2017). N-MORB normalizing data are from Sun and Mcdonough (1989).

single-lid episode during the "Boring Billion" of Earth history (Pearce & Reagan, 2019; Stern, 2020). For this reason there is no evidence for deformation and magmatism related to modern plate tectonics in the Mesoproterozoic, such as ophiolite, passive continental margins, blueschists, and ultra-high-pressure terranes (Stern, 2020). Global IBM-like subduction systems in the Neoproterozoic are temporally correlated with the appearance of volatile-bearing kimberlites, passive continental margin, plate tectonic gemstones (jadeite and ruby), and Alpine facies metamorphic series (glaucophane-bearing metamorphism), re-formation of orogenic gold, iron formation, and volcanic-hosted massive sulfide deposits (Figure 13; Stern et al., 2016; Zheng & Zhao, 2020), all of which demonstrate the onset of modern-style plate tectonics with cold and deep subduction. Therefore, in the latest Neoproterozoic, the single-lid tectonic regime may have evolved into modern-style plate tectonics as the Earth cooled.

Significantly, the Yangtze Block of South China, Arabian Shield, Nubian Shield, Siberia Craton, and India which have abundant Neoproterozoic ophiolites (Figure 13c) were located on the margin of the Rodinia supercontinent (ca. 850 Ma), in paleogeographic reconstructions, adjacent to the circum-continental supra-subduction zone (Merdith et al., 2017; K. L. Wang et al., 2017; Wang, Cawood, & Pandit, 2021; Wang, Cawood, Pandit, Xia, et al., 2021). The relatively rigid plate margin and low mantle temperature promoted
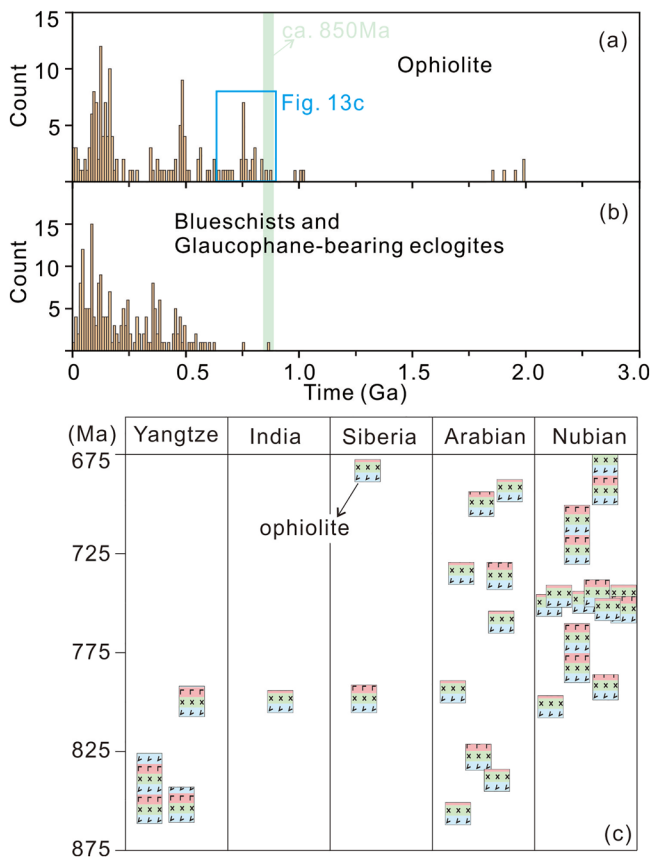
Figure 13. (a and b) Age histograms for ophiolite and deep subduction indicator of blueschist and glaucophane-bearing eclogites for the past 3 Ga (modified after compiled data from Furnes et al., 2014; Tsujimori & Ernst, 2014). (c) Spatial and temporal distribution of Neoproterozoic ophiolites (modified after compiled data from Furnes et al., 2014; Zhao et al., 2017).

cold and deep subduction along the Rodinia margins that likely induced mantle flow into a much wider cell resulting in extensional stresses at greater distances from the trench (e.g., ~3,000 km; Dal Zilio et al., 2018). This high and sustained sub-continental traction may exceed the strength of the continental lithosphere, and eventually lead to the breakup and opening of distal basin or mantle upwelling (Dal Zilio et al., 2018; Heron et al., 2015). Consequently, the initiation of Neoproterozoic cold and deep subduction around its periphery could be the geodynamic trigger of Rodinia breakup resulting in the full dispersal of the supercontinent (Cawood et al., 2016). This is in contrast to the partial breakup of Nuna/Columbia supercontinent in the late Paleoproterozoic to Mesoproterozoic, dominated by single-lid plate tectonics with warm and shallow subduction.

It should be noted that some boninites were developed in the Paleoproterozoic and/or Archean (>2.0 Ga), however, as evidenced below they appear not to have formed in a modern cold and deep slab subduction setting. These Archean-Paleoproterozoic boninites from greenstone belts show some similarities with those from forearc settings, such as the crustal rock assemblages of the Nuvvuagittuq supracrustal belt (≥ca. 3.8 Ga) in Quebec (Canada; Turner et al., 2014), whereas boninites from greenstone belts are generally associated with coeval komatiites, such as volcanic flows from the 2.7 Ga Abitibi greenstone belt (Kerrich et al., 1998) and the ca. 2.3 Ga Bogoin-Boali greenstone belt (Poidevin, 1994), indicating an alternative non-modern-style plate tectonics model (Davies, 1992). These may be products of locally failed subduction owing to ductile lithosphere margin and high mantle temperatures, which has been defined as warm and shallow subduction accompanied by ancient-style plate tectonics (Zheng & Zhao, 2020). In addition, numerical simulations of subduction in the Paleoproterozoic/Archean Earth also suggest that spreading ridges, transform faults, and subduction zones are predicted to be isolated in "microcells" at the head of mantle plumes under stagnant lid tectonics (Palin et al., 2020). Therefore, the boninite and minor ophiolites in the Paleoproterozoic and/or Archean (>2.0 Ga) here are considered as the product of ancient-style plate tectonics, which is controlled by both hot subduction and mantle plumes.

6. Conclusions

Our detailed studies of mineral geochemistry reveal that the Fuchuan ophiolite is analogous to the forearc oceanic stratigraphy sequence from the IBM subduction system. Physical conditions of high temperature (1,000–1,200°C), low pressure, high degrees of melts extraction (>18%) recorded in the Fuchuan harzburgite, suggest that forearc basalt and boninite are likely to have formed. Two types of clinopyroxene from the cumulate gabbro correspond to forearc basaltic magma (low Mg#) and boninite magma (high Mg#), respectively. Combined with previous work on the Fuchuan ophiolite, magma evolution from forearc basalt to boninite to hydrous calc-alkaline magmatism indicates a transition from initial to mature subduction in a forearc setting. Statistical analysis of global ophiolites suggests that IBM-like subduction systems may have successfully operated since at least the latest Neoproterozoic (ca. 1,000 Ma) and be pervasive in Earth from ca. 850 Ma. Neoproterozoic ophiolites from India, Siberia, and Arabian-Nubian Shield are also similar to IBM forearc ophiolite, suggesting that cold subduction and modern-style plate tectonics may have pervasively developed in the Neoproterozoic (ca. 850 Ma) around the periphery of the Rodinia supercontinent, and this may have acted as the geodynamic trigger for the full dispersal of Rodinia.

Data Availability Statement

Tables S1–S7 are included in Supporting Information S1 and all the data for this article are available from the Zenodo data set (https://doi.org/10.5281/zenodo.5336180).

References

Abdel Halim, A. H., Helmy, H. M., Elhaddad, M. A., El-Mahallawi, M. M., & Mogessie, A. (2020). Petrology of a Neoproterozoic mantle peridotite-chromitite association from Abu Dahr area, Eastern Desert, Egypt: Infiltration of a boninitic melt in highly depleted harzburgite. *Journal of African Earth Sciences*, *165*, 103816. https://doi.org/10.1016/j.jafrearsci.2020.103816

Abdel-Karim, A.-A. M., Ali, S., & El-Shafei, S. A. (2018). Mineral chemistry and geochemistry of ophiolitic metaultramafics from Um Halham and Fawakhir, Central Eastern Desert, Egypt. *International Journal of Earth Sciences*, *107*, 2337–2355. https://doi.org/10.1007/s00531-018-1601-2

Abuamarah, B. A. (2020). Geochemistry and fore-arc evolution of upper mantle peridotites in the Cryogenian Bir Umq ophiolite, Arabian Shield, Saudi Arabia. *International Geology Review*, *62*, 630–648. https://doi.org/10.1080/00206814.2019.1652942

Andersen, T. (2002). Correction of common lead in U-Pb analyses that do not report [204]Pb. *Chemical Geology*, *192*, 59–79. https://doi.org/10.1016/S0009-2541(02)00195-X

Ballhaus, C., Berry, R. R., & Green, D. H. (1991). High pressure experimental calibration of the olivine-orthopyroxene-spinel oxygen geobarometer: Implications for the oxidation state of the upper mantle. *Contributions to Mineralogy and Petrology*, *107*, 27–40. https://doi.org/10.1007/BF00310615

Bernstein, S., Kelemen, P. B., & Brooks, C. K. (1998). Depleted spinel harzburgite xenoliths in tertiary dykes from East Greenland: Restites from high degree melting. *Earth and Planetary Science Letters*, *154*, 221–235. https://doi.org/10.1016/S0012-821X(97)00175-1

Brey, G. P., & Köhler, T. (1990). Geothermobarometry in four-PHASE lherzolites II. New thermobarometers, and practical assessment of existing thermobarometers. *Journal of Petrology*, *31*, 1353–1378. https://doi.org/10.1093/petrology/31.6.1353

Cawood, P. A., Hawkesworth, C. J., Pisarevsky, S. A., Dhuime, B., Capitanio, F. A., & Nebel, O. (2018). Geological archive of the onset of plate tectonics. *Philosophical Transactions of the Royal Society*, *A376*, 20170405. https://doi.org/10.1098/rsta.2017.0405

Cawood, P. A., Strachan, R. A., Pisarevsky, S. A., Gladkochub, D. P., & Murphy, J. B. (2016). Linking collisional and accretionary orogens during Rodinia assembly and breakup: Implications for models of supercontinent cycles. *Earth and Planetary Science Letters*, *449*, 118–126. https://doi.org/10.1016/j.epsl.2016.05.049

Chen, X., Wang, D., Wang, X. L., Gao, J. F., Shu, X. J., Zhou, J. C., & Qi, L. (2014). Neoproterozoic chromite-bearing high-Mg diorites in the western part of the Jiangnan orogen, southern China: Geochemistry, petrogenesis and tectonic implications. *Lithos*, *200–201*, 35–48. https://doi.org/10.1016/j.lithos.2014.04.007

Coogan, L. A., Saunders, A. D., & Wilson, R. N. (2014). Aluminum-in-olivine thermometry of primitive basalts: Evidence of an anomalously hot mantle source for large igneous provinces. *Chemical Geology*, *368*, 1–10. https://doi.org/10.1016/j.chemgeo.2014.01.004

Coulthard, D. A., Reagan, M. K., Shimizu, K., Bindeman, I. N., Brounce, M., Almeev, R. R., et al. (2021). Magma source evolution following subduction initiation: Evidence from the element concentrations, stable isotope ratios, and water contents of volcanic glasses from the Bonin forearc (IODP expedition 352). *Geochemistry, Geophysics, Geosystems*, *22*, e2020GC009054. https://doi.org/10.1029/2020gc009054

Dal Zilio, L., Faccenda, M., & Capitanio, F. (2018). The role of deep subduction in supercontinent breakup. *Tectonophysics*, *746*, 312–324. https://doi.org/10.1016/j.tecto.2017.03.006

Dandar, O., Okamoto, A., Uno, M., Oyanagi, R., Nagaya, T., Burenjargal, U., et al. (2019). Formation of secondary olivine after orthopyroxene during hydration of mantle wedge: Evidence from the Khantaishir ophiolite, western Mongolia. *Contributions to Mineralogy and Petrology*, *174*, 86. https://doi.org/10.1007/s00410-019-1623-1

Dare, S. A. S., Pearce, J. A., McDonald, I., & Styles, M. T. (2009). Tectonic discrimination of peridotites using fO_2-Cr# and Ga-Ti-FeIII systematics in chrome-spinel. *Chemical Geology*, *261*, 199–216. https://doi.org/10.1016/j.chemgeo.2008.08.002

Davies, G. F. (1992). On the emergence of plate tectonics. *Geology*, *20*, 963–966. https://doi.org/10.1130/0091-7613(1992)020<0963:OTEOPT>2.3.CO;2

De Hoog, J. C. M., Gall, L., & Cornell, D. H. (2010). Trace-element geochemistry of mantle olivine and application to mantle petrogenesis and geothermobarometry. *Chemical Geology*, *270*, 196–215. https://doi.org/10.1016/j.chemgeo.2009.11.017

Dick, H., & Bullem, T. (1984). Chromian spinel as a petrogenetic indicator in abyssal and alpine-type peridotites and spatially associated lavas. *Contributions to Mineralogy and Petrology*, *86*, 54–76. https://doi.org/10.1007/bf00373711

Dijkstra, A., Brouwer, F., Cunningham, W., Buchan, C., Badarch, G., & Mason, P. R. D. (2006). Late Neoproterozoic proto-arc ocean crust in the Dariv Range, western Mongolia: A supra-subduction zone end-member ophiolite. *Journal of the Geological Society*, *163*, 363–373. https://doi.org/10.1144/0016-764904-156

Dilek, Y., & Furnes, H. (2011). Ophiolite genesis and global tectonics: Geochemical and tectonic fingerprinting of ancient oceanic lithosphere. *GSA Bulletin*, *123*, 387–411. https://doi.org/10.1130/b30446.1

Dilek, Y., & Furnes, H. (2014). Ophiolites and their origins. *Elements*, *10*, 93–100. https://doi.org/10.2113/gselements.10.2.93

Ding, B. H., Shi, R. D., Zhi, X. C., Zheng, L., & Chen, L. (2008). Neoproterozoic (~850Ma) subduction in the Jiangnan orogen: Evidence from the SHRIMP U-Pb dating of the SSZ-type ophiolite in southern Anhui Province. *Acta Petrologica et Mineralogica*, *27*, 375–388. (in Chinese with English Abstract).

El-Rahman, Y. A., Polat, A., Dilek, Y., Fryer, B. J., El-Sharkawy, M., & Sakran, S. (2009). Geochemistry and tectonic evolution of the Neoproterozoic incipient arc-forearc crust in the Fawakhir area, Central Eastern Desert of Egypt. *Precambrian Research*, *175*, 116–134. https://doi.org/10.1016/j.precamres.2009.09.008

Falloon, T. J., Danyushevsky, L. V., Crawford, T. J., Maas, R., Woodhead, J. D., Eggins, S. M., et al. (2007). Multiple mantle plume components involved in the petrogenesis of subduction-related lavas from the northern termination of the Tonga Arc and northern Lau Basin: Evidence from the geochemistry of arc and backarc submarine volcanics. *Geochemistry, Geophysics, Geosystems*, *8*, Q09003. https://doi.org/10.1029/2007gc001619

Farahat, E. S. (2010). Neoproterozoic arc-back-arc system in the Central Eastern Desert of Egypt: Evidence from supra-subduction zone ophiolites. *Lithos*, *120*, 293–308. https://doi.org/10.1016/j.lithos.2010.08.017

Farahat, E. S., Hoinkes, G., & Mogessie, A. (2011). Petrogenetic and geotectonic significance of Neoproterozoic suprasubduction mantle as revealed by the Wizer ophiolite complex, Central Eastern Desert, Egypt. *International Journal of Earth Sciences*, *100*, 1433–1450. https://doi.org/10.1007/s00531-010-0592-4

Furnes, H., de Wit, M., & Dilek, Y. (2014). Four billion years of ophiolites reveal secular trends in oceanic crust formation. *Geoscience Frontiers*, *5*, 571–603. https://doi.org/10.1016/j.gsf.2014.02.002

Gahlan, H. A., Azer, M. K., & Khalil, A. E. S. (2015). The Neoproterozoic Abu Dahr ophiolite, South Eastern Desert, Egypt: Petrological characteristics and tectonomagmatic evolution. *Mineralogy and Petrology*, *109*, 611–630. https://doi.org/10.1007/s00710-015-0397-z

Goodenough, K., Thomas, B., Styles, M., Schofield, D., & MacLeod, C. (2014). Records of ocean growth and destruction in the Oman-UAE ophiolite. *Elements*, *10*, 105–114. https://doi.org/10.2113/gselements.10.2.109

Hellebrand, E., Snow, J. E., Dick, H. J. B., & Hofmann, A. W. (2001). Coupled major and trace elements as indicators of the extent of melting in mid-ocean-ridge peridotites. *Nature*, *410*, 677–681. https://doi.org/10.1038/35070546

Heron, P. J., Lowman, J. P., & Stein, C. (2015). Influences on the positioning of mantle plumes following supercontinent formation. *Journal of Geophysical Research: Solid Earth*, *120*, 3628–3648. https://doi.org/10.1002/2014JB011727

Herzberg, C. (1992). Depth and degree of melting of komatiites. *Journal of Geophysical Research: Solid Earth*, *97*, 4521–4540. https://doi.org/10.1029/91JB03066

Herzberg, C. (2004). Geodynamic information in peridotite petrology. *Journal of Petrology*, *45*, 2507–2530. https://doi.org/10.1093/petrology/egh039

Hirose, K., & Kushiro, I. (1993). Partial melting of dry peridotites at high pressures: Determination of compositions of melts segregated from peridotite using aggregates of diamond. *Earth and Planetary Science Letters*, *114*, 477–489. https://doi.org/10.1016/0012-821X(93)90077-M

Holder, R. M., Viete, D. R., Brown, M., & Johnson, T. E. (2019). Metamorphism and the evolution of plate tectonics. *Nature*, *572*, 378–381. https://doi.org/10.1038/s41586-019-1462-2

Hu, M. Y., Fan, X. T., Stoll, B., Kuzmin, D., Liu, Y., Liu, Y., et al. (2011). Preliminary characterisation of new reference materials for microanalysis: Chinese geological standard glasses CGSG-1, CGSG-2, CGSG-4 and CGSG-5. *Geostandards and Geoanalytical Research*, *35*, 235–251. https://doi.org/10.1111/j.1751-908X.2010.00097.x

Huang, S. F., Wang, W., Pandit, M. K., Zhao, J. H., Lu, G. M., & Xue, E. K. (2019). Neoproterozoic S-type granites in the western Jiangnan Orogenic Belt, South China: Implications for petrogenesis and geodynamic significance. *Lithos*, *342–343*, 45–58. https://doi.org/10.1016/j.lithos.2019.05.016

Huang, S. F., Wang, W., Zhao, J. H., & Zheng, J. P. (2018). Petrogenesis and geodynamic significance of the ∼850 Ma Dongling A-type granites in South China. *Lithos*, *318–319*, 176–193. https://doi.org/10.1016/j.lithos.2018.08.016

Hussein, I. M., Kröner, A., & Reischmann, T. (2004). The Wadi Onib mafic-ultramafic complex: A Neoproterozoic supra-subduction zone ophiolite in the Northern Red Sea Hills of the Sudan. *Developments in Precambrian Geology*, *13*, 163–206. https://doi.org/10.1016/S0166-2635(04)13005-3

Ishikawa, T., Nagaishi, K., & Umino, S. (2002). Boninitic volcanism in the Oman ophiolite: Implications for thermal condition during transition from spreading ridge to arc. *Geology*, *30*, 899–902. https://doi.org/10.1130/0091-7613(2002)030<0899:bvitoo>2.0.co;2

Ishizuka, O., Kimura, J. I., Li, Y., Stern, B., Reagan, M., Taylor, R., et al. (2006). Early stages in the evolution of Izu-Bonin arc volcanism: New age, chemical, and isotopic constraints. *Earth and Planetary Science Letters*, *250*, 385–401. https://doi.org/10.1016/j.epsl.2006.08.007

Ishizuka, O., Tani, K., & Reagan, M. K. (2014). Izu-Bonin-Mariana forearc crust as a modern ophiolite analogue. *Elements*, *10*, 115–120. https://doi.org/10.2113/gselements.10.2.115

Kerrich, R., Wyman, D., Fan, J., & Bleeker, W. (1998). Boninite series: Low Ti-tholeiite associations from the 2.7 Ga Abitibi greenstone belt. *Earth and Planetary Sciences Letters*, *164*, 303–316. https://doi.org/10.1016/S0012-821X(98)00223-4

Khain, E., Bibikova, E., Kröner, A., Zhuravlev, D., Sklyarov, E., Fedotova, A., & Kravchenko-Berezhnoy, I. R. (2002). The most ancient ophiolite of the Central Asian fold belt: U-Pb and Pb-Pb zircon ages for the Dunzhugur Complex, Eastern Sayan, Siberia, and geodynamic implications. *Earth and Planetary Science Letters*, *199*, 311–325. https://doi.org/10.1016/S0012-821X(02)00587-3

Khan, M. A., Ishaq, K. M., Thomas, U., Liaqat, A., Kerr, A. C., Khalid, M., & Siddiqui, R. H. (2020). Genesis of manganese deposits in the Ali Khanzai block of the Zhob ophiolite, Pakistan: Inferences from geochemistry and mineralogy. *Journal of Earth Science*, *31*, 884–895. https://doi.org/10.1007/s12583-020-1337-3

Kim, S., Santosh, M., Park, N., & Kwon, S. (2011). Forearc serpentinite mélange from the Hongseong suture, South Korea. *Gondwana Research*, *20*, 852–864. https://doi.org/10.1016/j.gr.2011.01.012

König, S., Münker, C., Schuth, S., Luguet, A., Hoffmann, J. E., & Kuduon, J. (2010). Boninites as windows into trace element mobility in subduction zones. *Geochimica et Cosmochimica Acta*, *74*, 684–704. https://doi.org/10.1016/j.gca.2009.10.011

Kuzmichev, A., Kröner, A., Hegner, E., Liu, D., & Wan, Y. (2005). The Shishkhid ophiolite, northern Mongolia: A key to the reconstruction of a Neoproterozoic island-arc system in central Asia. *Precambrian Research*, *138*, 125–150. https://doi.org/10.1016/j.precamres.2005.04.002

Li, H. Y., Taylor, R. N., Prytulak, J., Kirchenbaur, M., Shervais, J. W., Ryan, J. G., et al. (2019). Radiogenic isotopes document the start of subduction in the Western Pacific. *Earth and Planetary Science Letters*, *518*, 197–210. https://doi.org/10.1016/j.epsl.2019.04.041

Li, Q. W., & Zhao, J. H. (2020). Amalgamation between the Yangtze and Cathaysia Blocks in South China: Evidence from the ophiolite geochemistry. *Precambrian Research*, *350*, 105893. https://doi.org/10.1016/j.precamres.2020.105893

Li, X. H., Li, W. X., Li, Z. X., Lo, C. H., Wang, J., Ye, M. F., & Yang, Y.-H. (2009). Amalgamation between the Yangtze and Cathaysia Blocks in South China: Constraints from SHRIMP U-Pb zircon ages, geochemistry and Nd–Hf isotopes of the Shuangxiwu volcanic rocks. *Precambrian Research*, *174*, 117–128. https://doi.org/10.1016/j.precamres.2009.07.004

Li, Y., Wang, G., Santosh, M., Wang, J., Dong, P., & Li, H. (2020). Subduction initiation of the SE Paleo-Asian Ocean: Evidence from a well preserved intra-oceanic forearc ophiolite fragment in central Inner Mongolia, North China. *Earth and Planetary Science Letters*, *535*, 116087. https://doi.org/10.1016/j.epsl.2020.116087

Liu, Y., Hu, Z., Gao, S., Günther, D., Xu, J., Gao, C., & Chen, H. (2008). In situ analysis of major and trace elements of anhydrous minerals by LA-ICP-MS without applying an internal standard. *Chemical Geology*, *257*, 34–43. https://doi.org/10.1016/j.chemgeo.2008.08.004

Liu, G., Qian, X., Li, J., Zi, J., Zhao, T., Feng, Q., et al. (2020). Geochronological and Geochemical Constraints on the Petrogenesis of Early Paleoproterozoic (2.40-2.32 Ga) Nb-Enriched Mafic Rocks in Southwestern Yangtze Block and Its Tectonic Implications. *Journal of Earth Science*, *31*(1), 35–52. https://doi.org/10.1007/s12583-020-1260-7

Ludwig, K. R. (2003). *User's manual for isoplot 3.00, a geolochronolgical toolkit for Microsoft Excel*. Berkeley Geochronology Center, Special Publication.

McDade, P., Blundy, J. D., & Wood, B. J. (2003a). Trace element partitioning between mantle wedge peridotite and hydrous MgO-rich melt. *American Mineralogist*, *88*, 1825–1831. https://doi.org/10.2138/am-2003-11-1225

McDade, P., Blundy, J. D., & Wood, B. J. (2003b). Trace element partitioning on the Tinaquillo Lherzolite solidus at 1.5 GPa. *Physics of the Earth and Planetary Interaction*, *139*, 129–147. https://doi.org/10.1016/S0031-9201(03)00149-3

Merdith, A. S., Collins, A. S., Williams, S. E., Pisarevsky, S., Foden, J. D., Archibald, D. B., et al. (2017). A full-plate global reconstruction of the Neoproterozoic. *Gondwana Research*, *50*, 84–134. https://doi.org/10.1016/j.gr.2017.04.001

Morishita, T., Tani, K., Shukuno, H., Harigane, Y., Tamura, A., Kumagai, H., & Hellebrand, E. (2011). Diversity of melt conduits in the Izu-Bonin-Mariana forearc mantle: Implications for the earliest stage of arc magmatism. *Geology*, *39*, 411–414. https://doi.org/10.1130/g31706.1

Ning, W., Wang, J., Xiao, D., Li, F., Huang, B., & Fu, D. (2019). Electron probe microanalysis of Monazite and its applications to U-Th-Pb dating of geological samples. *Journal of Earth Science*, *30*, 952–963. https://doi.org/10.1007/s12583-019-1020-8

Niu, Y. L. (2004). Bulk-rock major and trace element compositions of abyssal peridotites: Implications for mantle melting, melt extraction and post-melting processes beneath mid-ocean ridges. *Journal of Petrology*, *45*, 2423–2458. https://doi.org/10.1093/petrology/egh068

O'Neill, H. S. C., & Wall, V. J. (1987). The olivine-orthopyroxene-spinel oxygen geobarometer, the nickel precipitation curve, and the oxygen fugacity of the Earth's upper mantle. *Journal of Petrology*, *28*, 1169–1191. https://doi.org/10.1093/petrology/28.6.1169

Palin, R., Santosh, M., Cao, W., Li, S., Hernández-Uribe, D., & Parsons, A. (2020). Secular change and the onset of plate tectonics on Earth. *Earth-Science Reviews*, *207*, 103172. https://doi.org/10.1016/j.earscirev.2020.103172

Pearce, J. A., & Arculus, R. J. (2021). *Boninites, reference module in Earth systems and environmental sciences* (pp. 113–129). Elsevier. https://doi.org/10.1016/B978-0-08-102908-4.00152-1

Pearce, J. A., & Reagan, M. K. (2019). Identification, classification, and interpretation of boninites from Anthropocene to Eoarchean using Si-Mg-Ti systematics. *Geosphere*, *15*, 1008–1037. https://doi.org/10.1130/GES01661.1

Pearce, J. A., & Robinson, P. T. (2010). The Troodos ophiolitic complex probably formed in a subduction initiation, slab edge setting. *Gondwana Research*, *18*, 60–81. https://doi.org/10.1016/j.gr.2009.12.003

Peltonen, P., Kontinen, A., & Huhma, H. (1996). Petrology and geochemistry of metabasalts from the 1.95 Ga Jormua Ophiolite, Northeastern Finland. *Journal of Petrology*, *37*, 1359–1383. https://doi.org/10.1093/petrology/37.6.1359

Peng, S., Kusky, T., Jiang, X., Wang, L., Wang, J., & Deng, H. (2012). Geology, geochemistry, and geochronology of the Miaowan ophiolite, Yangtze craton: Implications for South China's amalgamation history with the Rodinian supercontinent. *Gondowana Research*, *21*, 577–594. https://doi.org/10.1016/j.gr.2011.07.010

Poidevin, J. L. (1994). Boninite-like rocks from the Palaeoproterozoic greenstone belt of Bogoin, Central African Republic: Geochemistry and petrogenesis. *Precambrian Research*, *68*, 97–113. https://doi.org/10.1016/0301-9268(94)90067-1

Putirka, K. D. (2008). Thermometers and barometers for volcanic systems. *Reviews in Mineralogy and Geochemistry*, *69*, 61–120. https://doi.org/10.2138/rmg.2008.69.3

Reagan, M. K., Heaton, D. E., Schmitz, M. D., Pearce, J. A., Shervais, J. W., & Koppers, A. (2019). Forearc ages reveal extensive short-lived and rapid seafloor spreading following subduction initiation. *Earth and Planetary Science Letters*, *506*, 520–529. https://doi.org/10.1016/j.epsl.2018.11.020

Reagan, M. K., Ishizuka, O., Stern, R. J., Kelley, K. A., Ohara, Y., Blichert-Toft, J., et al. (2010). Fore-arc basalts and subduction initiation in the Izu-Bonin-Mariana system. *Geochemistry, Geophysics, Geosystems*, *11*, Q03X12. https://doi.org/10.1029/2009gc002871

Reagan, M. K., Pearce, J. A., Petronotis, K., Almeew, R., Avery, A., Carvallo, C., et al. (2017). Subduction initiation and ophiolite crust: New insights from IODP drilling. *International Geology Review*, *59*, 1439–1450. https://doi.org/10.1080/00206814.2016.1276482

Resing, J., Rubin, K., Embley, R., Lupton, J., Baker, E., Dziak, R., et al. (2011). Active submarine eruption of boninite in the northeastern Lau Basin. *Nature Geoscience*, *4*, 799–806. https://doi.org/10.1038/ngeo1275

Rioux, M., Bowring, S., Kelemen, P., Gordon, S., Dudás, F., & Miller, R. (2012). Rapid crustal accretion and magma assimilation in the Oman-U.A.E. ophiolite: High precision U-Pb zircon geochronology of the gabbroic crust. *Journal of Geophysical Research: Solid Earth*, *117*, B07201. https://doi.org/10.1029/2012jb009273

Schwindinger, M., Weinberg, R. F., & White, R. W. (2020). The fate of accessory minerals and key trace elements during anatexis and magma extraction. *Journal of Petrology*, *61*, egaa031. https://doi.org/10.1093/petrology/egaa031

Scott, D., Helmstaedt, H., & Bickle, M. (1992). Purtuniq ophiolite, Cape smith belt, northern Quebec, Canada: A reconstructed section of Early Proterozoic oceanic crust. *Geology*, *20*, 173–176. https://doi.org/10.1130/0091-7613(1992)020<0173:POCSBN>2.3.CO;2

Shervais, J. W., Reagan, M., Haugen, E., Almeev, R. R., Pearce, J. A., Prytulak, J., et al. (2019). Magmatic response to subduction initiation: Part 1. Fore-arc basalts of the Izu-Bonin arc from IODP expedition 352. *Geochemistry, Geophysics, Geosystems*, *20*, 314–338. https://doi.org/10.1029/2018GC007731

Shervais, J. W., Reagan, M. K., Godard, M., Prytulak, J., Ryan, J. G., Pearce, J. A., et al. (2021). Magmatic response to subduction initiation, Part II: Boninites and related rocks of the IzuBonin Arc from IODP Expedition 352. *Geochemistry, Geophysics, Geosystems*, *22*, e2020GC009093. https://doi.org/10.1029/2020GC009093

Shi, H., Wang, J., Yao, Y., Zhang, J., Jin, S., Zhu, Y., et al. (2020). Geochemistry and Geochronology of Diorite in Pengshan Area of Jiangxi Province: Implications for Magmatic Source and Tectonic Evolution of Jiangnan Orogenic Belt. *Journal of Earth Science*, *31*(1), 23–34. https://doi.org/10.1007/s12583-020-0875-z

Shu, L., Wang, J., & Yao, J. (2019). Tectonic evolution of the eastern Jiangnan region, South China: New findings and implications on the assembly of the Rodinia supercontinent. *Precambrian Research*, *322*, 42–65. https://doi.org/10.1016/j.precamres.2018.12.007

Sklyarov, E. V., Kovach, V. P., Kotov, A. B., Kuzmichev, A. B., Lavrenchuk, A. V., Perelyaev, V. I., & Shchipansky, A. A. (2016). Boninites and ophiolites: Problems of their relations and petrogenesis of boninites. *Russian Geology and Geophysics*, *57*, 127–140. https://doi.org/10.1016/j.rgg.2016.01.009

Stern, R. A., Syme, E. C., Bailes, A. H., & Lucas, S. B. (1995). Paleoproterozoic (1.90-1.86 Ga) arc volcanism in the Flin Flon Belt, Trans-Hudson Orogen, Canada. *Contributions to Mineralogy and Petrology*, *119*, 117–141. https://doi.org/10.1007/BF00307276

Stern, R. J. (2005). Evidence from ophiolites, blueschists, and ultrahigh-pressure metamorphic terranes that the modern episode of subduction tectonics began in Neoproterozoic time. *Geology*, *33*, 557–560. https://doi.org/10.1130/G21365.1

Stern, R. J. (2020). The Mesoproterozoic Single-Lid Tectonic Episode: Prelude to Modern Plate Tectonics. *Geological Society of America Today*, *30*, 4–10. https://doi.org/10.1130/GSATG480A.1

Stern, R. J., Leybourne, M. I., & Tsujimori, T. (2016). Kimberlites and the start of plate tectonics. *Geology*, *44*, 799–802. https://doi.org/10.1130/g38024.1

Stern, R. J., Reagan, M., Ishizuka, O., Ohara, Y., & Whattam, S. (2012). To understand subduction initiation, study forearc crust: To understand forearc crust, study ophiolites. *Lithosphere*, *4*, 469–483. https://doi.org/10.1130/l183.1

Suhr, G., Seck, H. A., Shimizu, N., Günther, D., & Jenner, G. (1998). Infiltration of refractory melts into the lowermost oceanic crust: Evidence from dunite- and gabbro-hosted clinopyroxenes in the Bay of Islands Ophiolite. *Contributions to Mineralogy and Petrology*, *131*, 136–154. https://doi.org/10.1007/s004100050384

Sun, S. S., & Mcdonough, W. F. (1989). Chemical and isotopic systematics of oceanic basalts: Implications for mantle composition and processes. *Geological Society London Special Publications*, *42*, 313–345. https://doi.org/10.1144/GSL.SP.1989.042.01.19

Tang, Z., Wang, F., Zhou, H., Wu, X., Chen, Z., Hu, K., et al. (2020). Neoproterozoic (∼800 Ma) subduction of ocean-continent transition: Constraint from arc magmatic sequence in Kaihua, Western Zhejiang. *Journal of Earth Science*, *45*, 180–193. https://doi.org/10.3799/dqkx.2018.244

Tian, Y., Jin, W., Wang, J., Ke, Z., & Long, W. (2021). Provenance and tectonic setting of Lengjiaxi group in the Central Jiangnan Orogen: A case study of Huanghudong formation, Yueyang area. *Journal of Earth Science*, *46*, 1328–1348. https://doi.org/10.3799/dqkx.2020.101

Tian, Y., Wang, W., Wang, L., Li, X., Xie, G., & Huang, S. F. (2020). Age and petrogenesis of the Yingyangguan volcanic rocks: Implications on constraining the boundary between Yangtze and Cathaysia blocks, South China. *Lithos*, *376–377*, 105775. https://doi.org/10.1016/j.lithos.2020.105775

Torró, L., Proenza, J. A., Rojas-Agramonte, Y., Garcia-Casco, A., Yang, J. H., & Yang, Y. H. (2018). Recycling in the subduction factory: Archaean to Permian zircons in the oceanic Cretaceous Caribbean island-arc (Hispaniola). *Gondwana Research*, *54*, 23–37. https://doi.org/10.1016/j.gr.2017.09.010

Tsujimori, T., & Ernst, W. G. (2014). Lawsonite blueschists and lawsonite eclogites as proxies for palaeo-subduction zone processes: A review. *Journal of Metamorphic Geology*, *32*, 437–454. https://doi.org/10.1111/jmg.12057

Turner, S., Rushmer, T., Reagan, M., & Moyen, J. F. (2014). Heading down early on? Start of subduction on Earth. *Geology*, *42*, 139–142. https://doi.org/10.1130/g34886.1

Volpe, A., & Macdougall, J. (1990). Geochemistry and isotopic characteristics of mafic (Phulad Ophiolite) and related rocks in the Delhi Supergroup, Rajasthan, India: Implications for rifting in the Proterozoic. *Precambrian Research*, *48*, 167–191. https://doi.org/10.1016/0301-9268(90)90061-T

Wan, Z., Coogan, L. A., & Canil, D. (2008). Experimental calibration of aluminum partitioning between olivine and spinel as a geothermometer. *American Mineralogist*, *93*, 1142–1147. https://doi.org/10.2138/am.2008.2758

Wang, K. L., Chu, Z., Gornova, M. A., Dril, S., O'Reilly, S. Y., Lin, K.-Y., & O'Reilly, S. Y. (2017). Depleted SSZ-type mantle peridotites in proterozoic eastern Sayan ophiolites in Siberia. *Geodynamics and Tectonophysics*, *8*, 583–587. https://doi.org/10.5800/Gt-2017-8-3-0298

Wang, W., Cawood, P. A., & Pandit, M. K. (2021). India in the Nuna to Gondwana supercontinent cycles: Clues from the north Indian and Marwar Blocks. *American Journal of Science*, *321*, 83–117. https://doi.org/10.2475/01.2021.02

Wang, W., Cawood, P. A., Pandit, M. K., Xia, X., Raveggi, M., Zhao, J., et al. (2021). Fragmentation of South China from greater India during the Rodinia-Gondwana transition. *Geology*, *49*(2), 228–232. https://doi.org/10.1130/g48308.1

Wang, W., Cawood, P. A., Pandit, M. K., Zhao, J., & Zheng, J. (2019). No collision between Eastern and Western Gondwana at their northern extent. *Geology*, *47*(4), 308–312. https://doi.org/10.1130/g45745.1

Wang, W., Cawood, P. A., Zhou, M. F., Pandit, M. K., Xia, X. P., & Zhao, J. H. (2017). Low-δ^{18}O rhyolites from the Malani Igneous Suite: A positive test for South China and NW India linkage in Rodinia. *Geophysical Research Letters*, *44*, 10298–10305. https://doi.org/10.1002/2017GL074717

Wang, W., Zhou, M. F., Yan, D. P., Li, L., & Malpas, J. (2013). Detrital zircon record of Neoproterozoic active-margin sedimentation in the eastern Jiangnan Orogen, South China. *Precambrian Research*, *235*, 1–19. https://doi.org/10.1016/j.precamres.2013.05.013

Wang, X. L., Zhou, J. C., Wan, Y. S., Kitajima, K., Wang, D., Bonamici, C., et al. (2013). Magmatic evolution and crustal recycling for Neoproterozoic strongly peraluminous granitoids from southern China: Hf and O isotopes in zircon. *Earth and Planetary Science Letters*, *366*, 71–82. https://doi.org/10.1016/j.epsl.2013.02.011

Wang, Y., Zhang, Y., Cawood, P. A., Zhou, Y., Zhang, F., Yang, X., & Cui, X. (2019). Early Neoproterozoic continental arc system at the central Jiangnan Orogen, South China: Geochronological and geochemical constraints on the key igneous rock-association. *GSA Bulletin*, *132*, 638–654. https://doi.org/10.1016/j.precamres.2019.105367

Witt-Eickschen, G., & Seck, H. A. (1991). Solubility of Ca and Al in orthopyroxene from spinel peridotite: An improved version of an empirical geothermometer. *Contributions to Mineralogy and Petrology*, *106*, 431–439. https://doi.org/10.1007/BF00321986

Woelki, D., Regelous, M., Haase, K. M., Romer, R. H. W., & Beier, C. (2018). Petrogenesis of boninitic lavas from the Troodos Ophiolite, and comparison with Izu-Bonin-Mariana fore-arc crust. *Earth and Planetary Science Letters*, *498*, 203–214. https://doi.org/10.1016/j.epsl.2018.06.041

Wyman, D. A. (1999). Paleoproterozoic boninites in an ophiolite-like setting, Trans-Hudson Orogen, Canada. *Geology*, *27*, 455–458. https://doi.org/10.1130/0091-7613(1999)027<0455:PBIAOL>2.3.CO;2

Xiong, Q., Griffin, W. L., Zheng, J. P., Pearson, N. J., & O'Reilly, S. Y. (2017). Two-layered oceanic lithospheric mantle in a Tibetan ophiolite produced by episodic subduction of Tethyan slabs. *Geochemistry, Geophysics, Geosystems*, *18*, 1189–1213. https://doi.org/10.1002/2016gc006681

Xiong, Q., Griffin, W. L., Zheng, K. P., O'Reilly, S. Y., Pearson, N. J., Xu, B., & Belousova, E. A. (2016). Southward trench migration at ∼130-120 Ma caused accretion of the Neo-Tethyan forearc lithosphere in Tibetan ophiolites. *Earth and Planetary Science Letters*, *438*, 57–65. https://doi.org/10.1016/j.epsl.2016.01.014

Yamasaki, T., Maeda, J., & Mizuta, T. (2006). Geochemical evidence in clinopyroxenes from gabbroic sequence for two distinct magmatisms in the Oman ophiolite. *Earth and Planetary Science Letters*, *251*, 52–65. https://doi.org/10.1016/j.epsl.2006.08.027

Yang, J., Wu, W., Lian, D., & Rui, H. (2021). Peridotites, chromitites and diamonds in ophiolites. *Nature Reviews Earth and Environment*, *2*, 198–212. https://doi.org/10.1038/s43017-020-00138-4

Yao, J., Cawood, P. A., Shu, L., & Zhao, G. (2019). Jiangnan Orogen, South China: A ∼970–820 Ma Rodinia margin accretionary belt. *Earth-Science Reviews*, *196*, 102872. https://doi.org/10.1016/j.earscirev.2019.05.016

Yao, J., Shu, L., & Santosh, M. (2014). Neoproterozoic arc-trench system and breakup of the South China Craton: Constraints from N-MORB type and arc-related mafic rocks, and anorogenic granite in the Jiangnan orogenic belt. *Precambrian Research*, *247*, 187–207. https://doi.org/10.1016/j.precamres.2014.04.008

Zhang, J., Ding, X., Liu, Y., Zhang, H., Shi, C., & Zou, Y. (2020). Geochronology and Geochemistry of the 890 Ma I-Type Granites in the Southwestern Yangtze Block: Petrogenesis and Crustal Evolution. *Journal of Earth Science*, *31*(6), 1216–1228. https://doi.org/10.1007/s12583-020-1339-1

Zhang, C. L., Santosh, M., Zou, H. B., Li, H. K., & Huang, W. C. (2013). The Fuchuan ophiolite in Jiangnan Orogen: Geochemistry, zircon U-Pb geochronology, Hf isotope and implications for the Neoproterozoic assembly of South China. *Lithos*, *179*, 263–274. https://doi.org/10.1016/j.lithos.2013.08.015

Zhang, S. B., Wu, R. X., & Zheng, Y. F. (2012). Neoproterozoic continental accretion in South China: Geochemical evidence from the Fuchuan ophiolite in the Jiangnan orogen. *Precambrian Research*, *220–221*, 45–64. https://doi.org/10.1016/j.precamres.2012.07.010

Zhang, Y., Wang, Y., Geng, H., Zhang, Y., Fan, W., & Zhong, H. (2013). Early Neoproterozoic (∼850Ma) back-arc basin in the Central Jiangnan Orogen (Eastern South China): Geochronological and petrogenetic constraints from meta-basalts. *Precambrian Research*, *231*, 325–342. https://doi.org/10.1016/j.precamres.2013.03.016

Zhao, G. C., & Cawood, P. A. (2012). Precambrian geology of China. *Precambrian Research*, *222–223*, 13–54. https://doi.org/10.1016/j.precamres.2012.09.017

Zhao, J. H., & Asimow, P. D. (2014). Neoproterozoic boninite-series rocks in South China: A depleted mantle source modified by sediment-derived melt. *Chemical Geology*, *388*, 98–111. https://doi.org/10.1016/j.chemgeo.2014.09.004

Zhao, J. H., Asimow, P. D., Zhou, M. F., Zhang, J., Yan, D. P., & Zheng, J. P. (2017). An Andean-type arc system in Rodinia constrained by the Neoproterozoic Shimian ophiolite in South China. *Precambrian Research*, *296*, 93–111. https://doi.org/10.1016/j.precamres.2017.04.017

Zhao, J. H., & Zhou, M. F. (2013). Neoproterozoic high-Mg basalts formed by melting of ambient mantle in South China. *Precambrian Research*, *233*, 193–205. https://doi.org/10.1016/j.precamres.2013.04.017

Zhao, J. H., Zhou, M. F., Yan, D. P., Zheng, J. P., & Li, J. W. (2011). Reappraisal of the agesof Neoproterozoic strata in South China: No connection with the Grenvillianorogeny. *Geology*, *39*, 299–302. https://doi.org/10.1130/G31701.1

Zheng, Y. F., & Zhao, G. (2020). Two styles of plate tectonics in Earth's history. *Science Bulletin*, *65*, 329–334. https://doi.org/10.1016/j.scib.2018.12.029

Zhou, X., Zheng, J. P., Li, Y., Zhu, H., Griffin, W. L., & O'Reilly, S. Y., et al. (2021). Melt Migration and Interaction in a Dunite Channel System within Oceanic Forearc Mantle: The Yushigou Harzburgite–Dunite Associations, North Qilian Ophiolite (NW China). *Journal of Petrology*, *62*, egaa115. https://doi.org/10.1093/petrology/egaa115